Hindawi
International Transactions on Electrical Energy Systems
Volume 2022, Article ID 7280220, 20 pages
https://doi.org/10.1155/2022/7280220

Research Article

Decomposition-Coordination-Based Voltage Control for High Photovoltaic-Penetrated Distribution Networks under Cloud-Edge Collaborative Architecture

Xutao Han [1,2] **and Yajian Zhang** [1]

[1]*School of Mechatronic Engineering and Automation, Shanghai University, Shanghai, China*
[2]*School of Electrical and Information Engineering, Tianjin University, Tianjin, China*

Correspondence should be addressed to Yajian Zhang; zhang_ya_jian@shu.edu.cn

Received 4 October 2021; Accepted 16 December 2021; Published 31 January 2022

Academic Editor: Paulo Moisés Almeida Costa

With the integration of high proportional photovoltaics (PVs) into distribution networks, the superposition of uncertain output power of PVs and stochastic load demand fluctuations have posed a serious challenge to voltage stability. In this paper, a multitimescale decomposition-coordination-based voltage control method is proposed under the cloud-edge cooperative architecture. The distribution network is firstly decomposed into several subnetworks. In each subnetwork, the edge computing device is equipped to realize the distributed control and provide external computing resources for the cloud center. Then, a multitimescale control scheme containing the interval dispatch stage and the real-time time-window stage is proposed. In the interval dispatch stage, a cloud-edge collaborative calculation strategy considering balanced resource allocation is well designed to obtain the global optimal power flows and the corresponding reference operating points of the voltage control equipment. Meanwhile, in the real-time time-window stage, a consensus-based voltage correction mechanism under the optimal power flow boundary constraints is designed to avoid the voltage violations caused by unexcepted power fluctuations deviating from the representative scenarios. Simulation results with the improved 33-bus and IEEE 123-bus systems have demonstrated the effectiveness of our proposed method.

1. Introduction

The applications of photovoltaics (PVs) in distribution networks are an effective approach to deal with the carbon emissions and pollution problems of traditional fossil fuels [1, 2]. However, the uncertain PV outputs also have posed a serious challenge to the voltage stability in highly penetrated scenarios [3]. Due to comprehensively considering the time characteristic differences of discrete and continuous voltage control equipment, the multitimescale voltage control methods usually have better global voltage control performance compared with the traditional single timescale control methods, which have attracted the attention of the researchers [4–6].

The traditional multitimescale voltage control model and method is centralized formed and implement at the cloud control center. Zhang et al. [7] have proposed a centralized robust optimal method with three timescales. The on-load tap changers (OLTCs) and capacitor banks (CBs) are scheduled hourly, while the reference operating points of PV inverters are set every 15 min, and the real-time droop control is conducted. Xu et al. [8] have proposed a centralized stochastic programming method considering the simplified power fluctuation scenarios. To deal with the voltage deviations caused by the short-term power fluctuations deviating from the representative scenarios, a centralized double-timescale scheduling method for OLTCs, CBs, and PVs has been conducted. To maintain the voltage deviations within the allowable ranges, Alam et al. [9] have designed a centralized ESS charging-discharging strategy with the functions of long-timescale peak-load shifting and short-timescale power supply and demand balance. More similar works can be found in [10–14]. However, with the

increase of PV penetration proportion and the expansion of distribution network scale, the requirement of adequate communication, computation, and data storage resources in the centralized methods will lead to low solution efficiency and complex control operation problems [15].

To overcome the shortcomings in centralized methods, some researchers have proposed decentralized voltage control methods [16–18]. By parting a distribution network into serval subnetworks, the edge computing devices with data storage, analysis, and communication capabilities are equipped in each subnetwork to realize distributed and localized voltage control. Chai et al. [19] have proposed a two-stage deterministic voltage control strategy based on network partition. In the long-timescale stage, the power losses and voltage deviations are optimized based on the alternative direction method of multipliers (ADMM), while the short timescale autonomous optimization is adopted in each subnetwork without considering the uncertain PV output and load demand fluctuation. Li et al. [20] have proposed a distributed adaptive robust voltage control method to minimize power loss while keeping operating constraints under uncertain power fluctuation scenarios. However, the conservative robust optimization solutions make the power flow boundaries among subnetworks usually not optimal. Bazrafshan and Gatsis [21] have proposed a power stochastic programming scheme to jointly optimize the PV inverter outputs and programmable load demands. A fine decentralized algorithm is developed via ADMM that results in closed-form updates per bus and scenario, rendering it not suitable to implement with a limited number and performance of edge computing devices. More similar works can be found in [22–25]. However, there may exist frequent interregional power exchanges during the decentralized voltage control process, which may cause the suboptimal operations of distribution networks. In addition, in the existing distributed methods, the influences of limited computing resources of edge-side devices on the solving efficiency of the voltage control optimization models have not been considered. In a real distribution network, the edge-side devices should undertake some other applications (e.g., load frequency control [26], power forecasting [27], distribution network, and multimicrogrid joint optimization [28]) except for voltage control.

In general, the traditional completely centralized or decentralized control strategies are usually difficult to take into account both high computational efficiency and global optimality. In recent years, some scholars have introduced the concept of cloud-edge collaborative (CEC) architecture into distribution networks, such as power scheduling [29], stability operation control [30], load forecasting [31], and other applications. The significant advantage of the CEC architecture is that it uses the computing and analysis capabilities of edge-sides to provide distributed control and participate in the collaborative optimization process with the cloud-side control center to achieve efficient parallel solving of complex applications. However, as far as we know, there is still less work on distribution network voltage control under CEC architecture. Inspired by this, a novel multitimescale decomposition-coordination-based voltage control (DCVC) method is proposed under CEC architecture, containing the interval dispatch stage and real-time time-window stage. The main contributions are as follows:

(i) In the interval dispatch stage, to determine the optimal power flows and the corresponding optimal reference operating points of voltage control equipment under representative scenarios, the global optimization algorithm based on ADMM is designed. In addition, a CEC computing and communication resource scheduling mechanism considering resource allocation imbalance is well designed to guarantee satisfactory solving efficiency.

(ii) In the real-time time-window stage, to avoid the violate violations caused by unexcepted power fluctuations deviating from the representative scenarios, a consensus-based voltage correction mechanism is developed under the optimal power flow boundary constraints obtained by ADMM. Therefore, the undesirable interregional power exchanges and the corresponding adverse effects on the optimal power flows can be effectively avoided compared with the traditional distributed schemes.

The remainder of this paper is organized as follows. Section 2 introduces the basic architecture of the CEC-DCVC method. PV and ESS allocation strategy is proposed in Section 3. Sections 4 and 5 give the mathematical models as well as solving algorithms for two stages. Case studies are conducted and discussed in Section 6. The conclusion is given in Section 7.

2. Basic Architecture of CEC-DCVC Method

As shown in Figure 1, in our proposed DCVC method, the distribution network is firstly decomposed into a series of subnetworks. The edge computing devices with communication capabilities are equipped in each subnetwork to realize distributed control and provide computing resources for the cloud-side control center. To avoid suboptimal operating in the overall network due to unexcepted interregional power flows caused by the decentralized voltage control in subnetworks, the ADMM deployed in the cloud and edge sides is adopted to determine the optimal power flow boundaries among different subnetworks. Specifically, the obtained results of ADMM contain power flow boundary between arbitrary subnetwork a and b, which are given by $\boldsymbol{\pi}^{a,b}$, $\boldsymbol{\kappa}^{a,b}$, and $\boldsymbol{\kappa}^{b,a}$ as intermediate variables in cloud-side and edge-sides, respectively, as shown in Figure 1. Generally, the different kinds of voltage control equipment can be categorized into discrete ones (e.g., OLTCs and CBs) and continuous ones (e.g., ESSs and PVs). Under the decomposition-coordination framework, a parallel solving scheme for the ADMM considering the computing source constraints is developed. The reference operating points of all the discrete voltage control equipment in the distribution network are determined via conducting the cloud-side ADMM subproblem, while the reference operating points of continuous equipment in each subnetwork are obtained via conducting the edge-side ADMM subproblems. The states in neighboring subnetworks

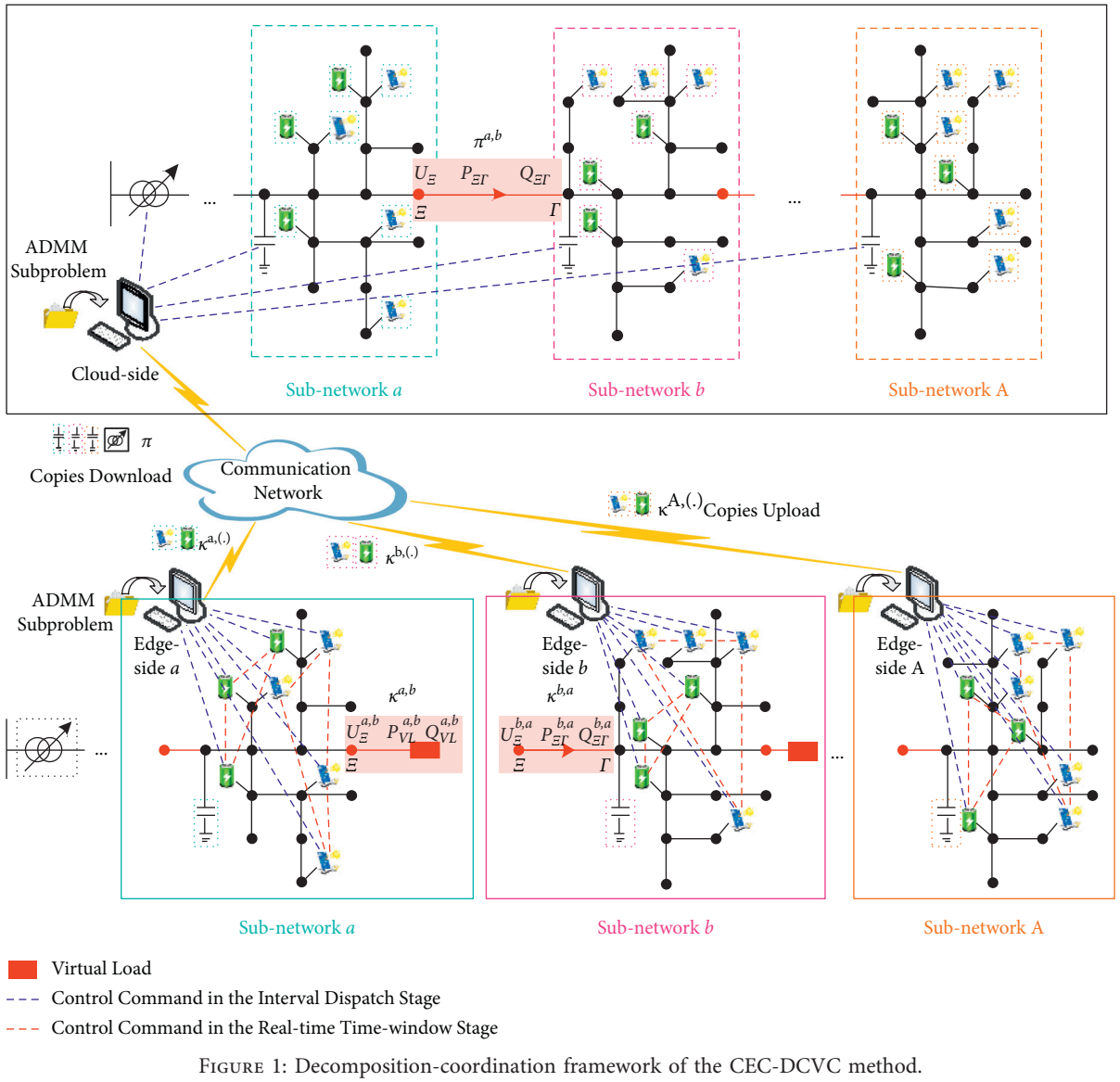

Figure 1: Decomposition-coordination framework of the CEC-DCVC method.

required to solve the ADMM are exchanged as a copy form through the communication network. When all the ADMM subproblems are converged, the final optimal power flow boundaries satisfy $\boldsymbol{\pi}^{a,b} = \boldsymbol{\kappa}^{a,b} = \boldsymbol{\kappa}^{b,a}$.

Further, the proposed DCVC voltage control method contains the following two stages with different timescales, as shown in Figure 2:

(i) Interval dispatch stage: according to the preset representative power fluctuation scenarios, the tap positions of discrete voltage equipment during the hourly interval and the reference operating points of continuous voltage equipment during the 15 min interval are determined by conducting the cloud and edge-side ADMM subproblems, respectively. Moreover, considering the influences of the computing and communication capability differences among the cloud-side control center and edge computing devices on the ADMM subproblem solving processes, a resource scheduling mechanism is well designed in this stage.

(ii) Real-time time-window stage: the unexpected power fluctuation deviating from the preset scenarios may cause voltage violation risks. Therefore, a consensus-based cluster correction scheme considering the optimal power flow boundary constraints is developed and deployed in the edge computing devices to realize real-time power regulations of the continuous voltage control equipment.

3. PV and ESS Allocation Strategy

Allocating PVs and ESSs based on the appropriate distribution network partition can reduce the whole network power loss while ensuring the subnetwork control capability. Therefore, this article innovatively builds a bilayer optimization model to achieve optimized allocation.

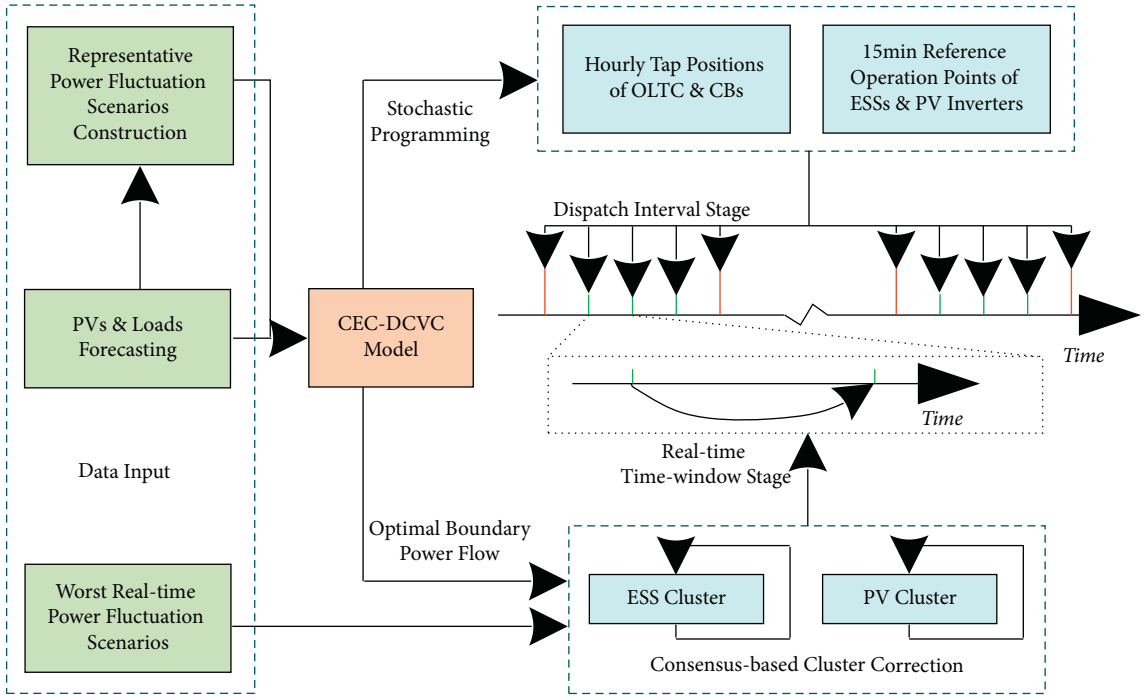

Figure 2: Multitimescale control realization based on the CEC-DCVC model.

3.1. PV and ESS Allocation Bilayer Optimization Model. The inner objective is to maximize subnetwork voltage control capability, as given in equation (1). The ESS and PV inverter constraints in each subnetwork are given in Appendix B equations (B.7)–(B.10). In addition, based on the concept of electrical distance between arbitrary two buses proposed by Chai [19], the lower and upper bounds of inside and outside electrical coupling strength are formed, respectively. Furthermore, the upper information propagation delay bound constraint in the real-time time-window stage is also sufficiently considered.

$$\max_{\mathbf{B}^a} \sum_{a\in\mathbf{A}} \sum_{e\in\mathbf{B}^a} h_e,$$

$$h_e = \begin{cases} 1, & \dfrac{\sum_{i\in\mathbf{B}^{a,\mathrm{ESS}}} P_i^{\mathrm{ESS}} S_{ie}^P + \sum_{j\in\mathbf{B}^{a,PV}} Q_j^{\mathrm{PV}} S_{je}^Q}{\Delta U_e^{\mathrm{ave}}} \geq 1, \\ \dfrac{\sum_{i\in\mathbf{B}^{a,\mathrm{ESS}}} P_i^{\mathrm{ESS}} S_{ie}^P + \sum_{j\in\mathbf{B}^{a,PV}} Q_j^{\mathrm{PV}} S_{je}^Q}{\Delta U_e^{\mathrm{ave}}}, & \text{otherwise}, \end{cases} \tag{1}$$

where $\mathbf{A}$ is the set of subnetworks; $\mathbf{B}^a$ represents the bus set of subnetwork a; h_e represents the ESS and PV control ability to bus e in subnetwork a; $\mathbf{B}^{a,\mathrm{ESS}}$ and $\mathbf{B}^{a,\mathrm{PV}}$ are the bus sets of ESS and PV clusters in subnetwork a respectively; P_i^{ESS} and Q_j^{PV} are the active and reactive power output of ESS and PV at bus i and bus j respectively; S_{ie}^P and S_{je}^Q are the active and reactive power sensitivity of bus i and bus j to bus e respectively; and $\Delta U_e^{\mathrm{ave}}$ represents the historical average voltage deviation of bus e.

3.1.1. Electrical Coupling Strength Constraints

$$\sum_{ij\in\mathbf{E}^a} \left(D_{ij}^P + D_{ij}^Q\right) \leq D^{\mathrm{in}}, \quad \forall a \in \mathbf{A}, \tag{2}$$

$$D^{\mathrm{out}} \leq \sum_{j\in\mathbf{B}^a} \left(D_{1j}^P + D_{1j}^Q\right), \quad \forall a \in \mathbf{A}, \tag{3}$$

$$\begin{bmatrix} D_{ij}^P \\ D_{ij}^Q \end{bmatrix} = \begin{bmatrix} S_{ii}^P \\ S_{ii}^Q \end{bmatrix} + \begin{bmatrix} S_{jj}^P \\ S_{jj}^Q \end{bmatrix} - \begin{bmatrix} S_{ij}^P \\ S_{ij}^Q \end{bmatrix} - \begin{bmatrix} S_{ji}^P \\ S_{ji}^Q \end{bmatrix}, \tag{4}$$

where $\mathbf{E}^a$ is the branch set of subnetwork a; D_{ij}^P and D_{ij}^Q are the active and reactive electrical distances from bus i and bus j respectively; and D^{in} and D^{out} represent the lower and upper bounds of inside and outside electrical coupling strength for subnetwork a respectively.

3.1.2. Information Propagation Delay Constraint

$$t_{\mathrm{delay}}^{a,\mathrm{ESS/PV}} = \frac{\log\left(N^{a,\mathrm{ESS/PV}} - 1\right)}{\log d^{a,\mathrm{ESS/PV}}} \left(t_{\mathrm{comp}}^{a,\mathrm{ESS/PV}} + t_{\mathrm{comm}}^{a,\mathrm{ESS/PV}} + t_{\mathrm{action}}^{a,\mathrm{ESS/PV}}\right) \leq \bar{t}_{\mathrm{delay}}, \quad \forall a \in \mathbf{A}, \tag{5}$$

where $t_{\mathrm{delay}}^{a,\mathrm{ESS/PV}}$ represents the ESS or PV cluster internal information propagation delay in subnetwork a; $N^{a,\mathrm{ESS/PV}}$ is the number of devices in ESS or PV cluster; the average communication point connectivity degree $d^{a,\mathrm{ESS/PV}}$ represents the information propagation ability; the ratio of two "log(·)" function represents the average hop counts required

to propagate the leading device status to all follower devices; $t_{\text{comp}}^{a,\text{ESS/PV}}$, $t_{\text{comm}}^{a,\text{ESS/PV}}$, and $t_{\text{action}}^{a,\text{ESS/PV}}$ represent the single communication, calculation, and action time of ESS or PV, respectively; and $\overline{t}_{\text{delay}}$ is the delay upper bound.

The outer objective function is to minimize the whole distribution network power loss. The power flow constraints of the whole distribution network are given in Appendix A equations (A.1)–(A.4), which have been preprocessed by second-order cone relaxation [32] to convert original nonconvex programming into convex programming. Embedding the inner function equation (1) into the outer function, the bilevel optimization model can be formed as follows:

$$\begin{cases} \min\limits_{\mathbf{B}^{\text{ESS}},\mathbf{B}^{\text{PV}}} \left(\sum\limits_{ij\in\mathbf{E}} l_{ij} r_{ij} \right) \max\limits_{\mathbf{B}^a} \sum\limits_{a\in\mathbf{A}} \sum\limits_{e\in\mathbf{B}^a} h_e, \\ \text{s.t. (A.1)} - \text{(A.4)}, \text{(B.7)} - \text{(B.10)}, \text{(2)} - \text{(5)}, \end{cases} \tag{6}$$

where $\mathbf{B}^{\text{ESS}}$ and $\mathbf{B}^{\text{PV}}$ are the bus sets of ESSs and PVs in the whole distribution network, respectively; $\mathbf{E}$ is the branch set of the whole distribution network; $l_{ij,t}$ is the square of current for branch ij; r_{ij} represents the resistance of branch ij.

3.2. Solving Process by Tabu Search Algorithm. Tabu search algorithm is applied in this paper to search for the optimal ESSs and PVs allocation strategy corresponding to the model (6). The dimension of $\mathbf{B}^{\text{ESS}}$ or $\mathbf{B}^{\text{PV}}$ is related to the number of buses in the distribution network, and each element of $\mathbf{B}^{\text{ESS}}$ or $\mathbf{B}^{\text{PV}}$ is "1" or "0." The number "1" indicates that ESS or PV is distributed to this bus, while the number "0" indicates the opposite. The neighbors of $\mathbf{B}^{\text{ESS}}$ or $\mathbf{B}^{\text{PV}}$ can be generated by changing several elements of $\mathbf{B}^{\text{ESS}}$ or $\mathbf{B}^{\text{PV}}$ from "1" to "0," or vice versa. Especially, the optimal solution is obtained based on the inner distribution network partition function equation (1). Finally, the detailed steps of Tabu search are shown in Algorithm 1.

4. Interval Dispatch Stage

To achieve the economic and safe operation of the distribution network under representative power fluctuation scenarios, the cloud and edge sides minimize the power loss of the whole network and the voltage deviations of subnetworks, respectively. Correspondingly, ADMM is adopted to solve the subproblems assigned to cloud and edge sides. Besides, the optimal power flow boundaries among subnetworks are formed.

4.1. Problem Descriptions

4.1.1. Cloud-Side Optimization Model. The optimization objective at the cloud-side is to minimize the power loss of the whole distribution network. The power flow, OLTC, and CB constraints of the whole network are given in Appendix A. The cloud-side optimization model can be described as

$$\begin{cases} \min\limits_{\boldsymbol{\alpha},\boldsymbol{\beta}} \sum\limits_{t\in\mathbf{T}^{\text{cloud}}} \Delta t \sum\limits_{ij\in\mathbf{E}} l_{ij,t} r_{ij}, \\ \text{s.t. (A.1)} - \text{(A.13)}, \\ \overline{\pi}^{a,b} \le \boldsymbol{\pi}^{a,b} \le \overline{\pi}^{a,b}, \quad a \in \mathbf{A}, b \in \mathbf{A}^a, \\ \boldsymbol{\pi}^{a,b} = \boldsymbol{\kappa}^{a,b}, \quad a \in \mathbf{A}, b \in \mathbf{A}^a, \end{cases} \tag{7}$$

where $\boldsymbol{\alpha}$ and $\boldsymbol{\beta}$ are the OLTC and CB state matrixes, respectively; $\mathbf{T}^{\text{cloud}}$ is the interval dispatch set at cloud-side; $\boldsymbol{\pi}^{a,b} = [U_\Xi, P_{\Gamma\Gamma}, Q_{\Gamma\Gamma}]$, U_Ξ is the voltage of boundary bus Ξ in arbitrary subnetwork a; $P_{\Gamma\Gamma}$ and $Q_{\Gamma\Gamma}$ are the active and reactive power of boundary branch $\Gamma\Gamma$ respectively; $\underline{\pi}^{a,b}$ and $\overline{\pi}^{a,b}$ are the lower bound and upper bound for power flow boundary, respectively; $\kappa^{a,b} = [U_\Xi^{a,b}, P_{\text{VL}}^{a,b}, Q_{\text{VL}}^{a,b}]$, $U_\Xi^{a,b}$ represents the hypothetical voltage of bus Ξ in subnetwork a; $P_{\text{VL}}^{a,b}$ and $Q_{\text{VL}}^{a,b}$ are the active and reactive power of virtual load, respectively; and $\mathbf{A}^a$ is the set of subnetworks adjacent to subnetwork a.

4.1.2. Edge-Side Optimization Model. The optimization objective at each edge-side is to minimize the voltage deviations in each subnetwork. The power flow, ESS, and PV inverter constraints in each subnetwork are given in Appendix B. To keep the same second-order cone forms in the cloud-side optimization model (7), the voltage deviation of arbitrary bus j is also expressed with the square form. The edge-side optimization model in each subnetwork can be described as

$$\begin{cases} \min\limits_{\mathbf{P}^{a,\text{ESS}},\mathbf{Q}^{a,\text{PV}}} \sum\limits_{t\in\mathbf{T}^{\text{edge}}} \sum\limits_{j\in\mathbf{B}^a} \dfrac{\left| u_{j,t} - U_0^2 \right|}{U_0^2}, \quad \forall a \in \mathbf{A}, \\ \text{s.t. (B.1)} - \text{(B.10)}, \\ \boldsymbol{\kappa}^{a,b} = \boldsymbol{\kappa}^{b,a}, \quad a \in \mathbf{A}, b \in \mathbf{A}^a, \end{cases} \tag{8}$$

where $\mathbf{P}^{a,\text{ESS}}$ is the discharge power matrix of ESSs; $\mathbf{Q}^{a,\text{PV}}$ is the reactive power output matrix of PV inverters; $\mathbf{T}^{\text{edge}}$ represents the interval dispatch set at edge-side; $u_{j,t}$ is the square of voltage amplitude for bus j; U_0^2 is square of the reference voltage amplitude; $\kappa^{b,a} = [U_\Xi^{b,a}, P_{\Xi\Gamma}^{b,a}, Q_{\Xi\Gamma}^{b,a}]$, $U_\Xi^{b,a}$ represents the hypothetical voltage of bus Ξ in subnetwork b; $P_{\Xi\Gamma}^{b,a}$ and $Q_{\Xi\Gamma}^{b,a}$ are the hypothetical active and reactive power of branch $\Gamma\Gamma$ respectively.

4.1.3. Stochastic Programming considering Power Fluctuations. In practice, the stochastic fluctuations of PV active power outputs and load demands may make it hard to sustain the power flows within the economic and safe boundaries by directly solving the above deterministic optimization models. Therefore, the optimization objectives of models (7) and (8) are further transferred into the following stochastic programming forms:

Initialize: $\mathbf{B}^{\mathrm{ESS}} = \mathbf{0}$, $\mathbf{B}^{\mathrm{PV}} = \mathbf{0}$, $k = 0$
[Edge-sides]: Calculate D_{ij}^{P} and D_{ij}^{Q} via equation (4)
Repeat:
  [Cloud-side]: Add $\mathbf{B}_k^{\mathrm{ESS}}$ and $\mathbf{B}_k^{\mathrm{PV}}$ into Tabu list and generate neighborhood list
  Repeat:
    Select candidate solutions from the neighborhood list
    If, ESSs and PVs in $\mathbf{B}^{a,\mathrm{ESS}}$ and $\mathbf{B}^{a,\mathrm{PV}}$ satisfy equations (B.7)–(B.10) and equation (5), buses in $\mathbf{B}^{a}$ satisfy equations (2)–(4)
      [Edge-sides]: Partition distribution network by solving equation (1)
      [Cloud-side]: Solve model (6) constrained by equations (A.1)–(A.4)
  Until local optimum is no longer updated
  [Cloud-side]: Set local optimum as $\mathbf{B}_{k+1}^{\mathrm{ESS}}$ and $\mathbf{B}_{k+1}^{\mathrm{PV}}$
  If the local optimum is better than the global optimum
    [Cloud-side]: Set the local optimum as the global optimum
Until maximum iteration

Algorithm 1: Tabu search for the optimal ESS and PV allocations based on subnetwork partition.

$$\begin{cases} \min\limits_{\mathbf{x}} E_{\boldsymbol{\xi}}\left(f^{\mathrm{loss}}\left(\mathbf{x}, \boldsymbol{\xi}, \widehat{\mathbf{y}}\right)\right), \\ \min\limits_{\mathbf{y}^a} E_{\boldsymbol{\xi}^a}\left(f^{a,|\Delta u|}\left(\widehat{\mathbf{x}}^a, \boldsymbol{\xi}^a, \mathbf{y}^a\right)\right), \quad \forall a \in \mathbf{A}, \end{cases} \tag{9}$$

where $\mathbf{x} = [\boldsymbol{\alpha}, \boldsymbol{\beta}]$; $\mathbf{y}^a = [\mathbf{P}^{a,\mathrm{ESS}}, \mathbf{Q}^{a,\mathrm{PV}}]$; $\boldsymbol{\xi} = \{\boldsymbol{\xi}^a \mid a \in \mathbf{A}\}$ is the set of PV active power outputs (denoted as $P_{j,t}^{\mathrm{PV}}$) and load demands (denoted as $Q_{j,t}^{\mathrm{load}}$); $E_{\boldsymbol{\xi}}(\cdot)$ and $E_{\xi}^{a}(\cdot)$ are the mathematical expectation under $\boldsymbol{\xi}$ and $\boldsymbol{\xi}^a$ respectively; $f^{\mathrm{loss}}(\cdot)$ and $f^{a,|\Delta u|}(\cdot)$ represent the objective of models (7) and (8) respectively; $\widehat{x}^a$ is the partial copy of $\mathbf{x}$ download to edge-side a; $\widehat{y} = [\widehat{y}^a]_{1\times A}$ is the summary of copies $\mathbf{y}^a$ upload to cloud-side; and A is the number of subnetworks.

Moreover, to solve the above stochastic programming equation (9), the uncertain variable $\boldsymbol{\xi}^a$ is simplified into a series of typical values with specific probabilities as Gaussian and Beta distribution [8]. Then, the representative scenario set $\mathbf{W}^a$ in subnetwork a can be described by the Cartesian product of PV output set $\mathbf{W}^{a,\mathrm{PV}}$ and load demand set $\mathbf{W}^{a,\mathrm{load}}$:

$$\mathbf{W}^a = \mathbf{W}^{a,\mathrm{PV}} \times \mathbf{W}^{a,\mathrm{load}} = \left\{\mathbf{w}^a = \left(\boldsymbol{\xi}^{\mathbf{w}^a}, \phi^{\mathbf{w}^a}\right)\right\}, \tag{10}$$

where $\xi^{\mathbf{w}^a}$ and $\phi^{\mathbf{w}^a}$ are uncertain variable and corresponding occurrence probability of scenario $\mathbf{w}^a$ respectively.

Correspondingly, the representative scenario set (denoted as $\mathbf{W}$) of the overall distribution network is given by

$$\mathbf{W} = \prod_{a\in\mathbf{A}} \mathbf{W}^a = \left\{\mathbf{w} = \left(\boldsymbol{\xi}^{\mathbf{w}}, \phi^{\mathbf{w}}\right)\right\}, \tag{11}$$

where $\phi^{\mathbf{w}} = \prod_{a\in\mathbf{A}} \phi^{\mathbf{w}^a}$ and $\xi^{w} = \left\{\xi^{w^a} | a \in \mathbf{A}\right\}$. Moreover, the stochastic programming equation (9) is retransferred into the following deterministic form:

$$\begin{cases} \min\limits_{\mathbf{x}} \sum\limits_{\mathbf{w}\in\mathbf{W}} \phi^{w} f^{\mathrm{loss}}\left(\mathbf{x}, \boldsymbol{\xi}^{w}, \widehat{\mathbf{y}}\right), \\ \min\limits_{\mathbf{y}^a} \sum\limits_{\mathbf{w}^a\in\mathbf{W}^a} \phi^{w^a} f^{a,|\Delta u|}\left(\widehat{\mathbf{x}}^a, \boldsymbol{\xi}^{\mathbf{w}^a}, \mathbf{y}^a\right), \quad \forall a \in \mathbf{A}. \end{cases} \tag{12}$$

4.2. ADMM-Based Optimization Procedure under CEC Architecture. According to equation (12), the number of optimization models is $A + 1$. To determine the optimal reference operating points of the voltage control equipment, all the cloud and edge-side optimization models should converge, which means that there exist frequent copy interactions during the optimization process. To guarantee the fast convergence in the interval dispatch stage, the ADMM considering computing resource constraints is adopted in the cloud-side control center and edge computing devices. Firstly, based on the augmented Lagrange function method, the cloud and edge side optimization models with equality constraint $\pi^{a,b} = \kappa^{a,b} = \kappa^{b,a}$ are further decoupled into $A + 1$ convex optimization models as follows:

$$\begin{cases} \min \varphi(\mathbf{x}), \\ \varphi(\mathbf{x}) = \sum\limits_{\mathbf{w}\in\mathbf{W}} \phi^{w} f^{\mathrm{loss}}\left(\mathbf{x}, \boldsymbol{\xi}^{\mathbf{w}}, \widehat{\mathbf{y}}\right) + \boldsymbol{\lambda}^{\mathrm{T}}\left(\boldsymbol{\pi}^{\mathrm{ave}} - \boldsymbol{\Omega}\right) + \dfrac{\rho}{2}\left\|\boldsymbol{\pi}^{\mathrm{ave}} - \boldsymbol{\Omega}\right\|_2^2, \\ \text{s.t. (A.1)} - \text{(A.13)}, \\ \underline{\boldsymbol{\pi}}^{a,b} \le \boldsymbol{\pi}^{a,b} \le \underline{\boldsymbol{\pi}}^{a,b}, \quad a \in \mathbf{A}, b \in \mathbf{A}^a, \end{cases} \tag{13}$$

$$\begin{cases} \min \psi(\mathbf{y}^a), \\ \psi(\mathbf{y}^a) = \sum\limits_{\mathbf{w}^a \in \mathbf{W}^a} \phi^{w^a} f^{a,|\Delta u|}\left(\widehat{\mathbf{x}}^a, \boldsymbol{\xi}^{w^a}, \mathbf{y}^a\right) + \sum\limits_{b \in \mathbf{A}^a}\left(\left(\boldsymbol{\lambda}^{a,b}\right)^{\mathrm{T}}\left(\boldsymbol{\kappa}^{\mathrm{ave},a,b} - \boldsymbol{\Omega}^{a,b}\right)\right) + \dfrac{\rho^a}{2}\left\|\boldsymbol{\kappa}^{\mathrm{ave},a,b} - \boldsymbol{\Omega}^{a,b}\right\|_2^2, \quad \forall a \in \mathbf{A}, b \in \mathbf{A}^a, \\ \text{s.t. (B.1)} - \text{(B.10)}, \end{cases} \tag{14}$$

where $\varphi(\cdot)$ and $\psi(\cdot)$ are the optimization functions at cloud and edge sides, respectively; $\pi^{\mathrm{ave}} = \sum_{\mathbf{w} \in \mathbf{W}} \phi^{\mathbf{w}} \pi^{\mathbf{w}}$, $\boldsymbol{\pi}^{\mathbf{w}}$ represents $\boldsymbol{\pi}$ under scenario $\mathbf{w}$; $\kappa^{\mathrm{ave},a,b} = \sum_{\mathbf{w}^a \in \mathbf{W}^a} \phi^{\mathbf{w}^a} \kappa^{\mathbf{w}^a,a,b}$, $\kappa^{\mathbf{w}^a,a,b}$ represents $\boldsymbol{\kappa}^{a,b}$ under scenario $\mathbf{w}^a$; for the whole network and subnetwork a respectively, $\boldsymbol{\Omega} = [\boldsymbol{\Omega}^{a,b}]_{1 \times L}$ and $\boldsymbol{\Omega}^{a,b}$ are the auxiliary variables, $\boldsymbol{\lambda}$ and $\boldsymbol{\lambda}^{a,b}$ are the dual variables, ρ and ρ^a are the penalty factors, and L is the number of power flow boundaries.

The update rules of $\boldsymbol{\Omega} = [\boldsymbol{\Omega}^{a,b}]_{1 \times L}$, $\boldsymbol{\lambda}$, and $\boldsymbol{\lambda}^{a,b}$ in the k^{th} iteration are given by

$$\begin{aligned} \boldsymbol{\Omega}_k &= \left[\boldsymbol{\Omega}_k^{a,b}\right]_{1 \times L} \\ &= \left[\frac{\boldsymbol{\pi}_{k-1}^{\mathrm{ave},a,b} + \boldsymbol{\kappa}_{k-1}^{\mathrm{ave},a,b} + \boldsymbol{\kappa}_{k-1}^{\mathrm{ave},b,a}}{3}\right]_{1 \times L}, \quad \forall a \in \mathbf{A}, b \in \mathbf{A}^a, \end{aligned} \tag{15}$$

$$\boldsymbol{\lambda}_k = \boldsymbol{\lambda}_{k-1} + \rho\left(\boldsymbol{\pi}_k^{\mathrm{ave}} - \boldsymbol{\Omega}_k\right), \tag{16}$$

$$\boldsymbol{\lambda}_k^{a,b} = \boldsymbol{\lambda}_{k-1}^{a,b} + \rho^a\left(\boldsymbol{\kappa}_k^{\mathrm{ave},a,b} - \boldsymbol{\Omega}_k^{a,b}\right), \quad \forall a \in \mathbf{A}, b \in \mathbf{A}^a, \tag{17}$$

The update rules of $\widehat{\mathbf{x}}$ and $\widehat{\mathbf{y}}^a$ in k^{th} iteration are given by

$$\widehat{\mathbf{x}}_k = \left[\widehat{x}_k^a\right]_{1 \times A} = \arg\min \varphi\left(\mathbf{x}_k\right), \tag{18}$$

$$\widehat{\mathbf{y}}_k^a = \arg\min \psi\left(\mathbf{y}_k^a\right), \quad \forall a \in \mathbf{A}. \tag{19}$$

The convergence criterion of ADMM is codetermined by the primary residual R_k and dual residual S_k in the cloud-side as follows:

$$\begin{cases} R_k = \left\|\boldsymbol{\pi}_k^{\mathrm{ave}} - \boldsymbol{\Omega}_k\right\|_\infty \le \varepsilon^{\mathrm{pri}}, \\ S_k = \rho\left\|\boldsymbol{\Omega}_k - \boldsymbol{\Omega}_{k-1}\right\|_\infty \le \varepsilon^{\mathrm{dual}}, \end{cases} \tag{20}$$

where $\varepsilon^{\mathrm{pri}}$ and $\varepsilon^{\mathrm{dual}}$ are the maximum allowable error of R_k and S_k respectively.

4.3. Solution Process with Computing and Communication Resource Scheduling. As shown in Figure 3, when the allocated computing and communication resources do not match the ADMM, only after $t_{\mathrm{imbalance}}^{\mathrm{edge,max}}$ all edge-sides have completed the subproblems and uploaded the copies to the cloud-side, the subproblem at the cloud-side can be executed. Similarly, each edge-side subproblem can only be calculated after $t_{\mathrm{imbalance}}^{\mathrm{cloud}}$ that the cloud-side has completed the subproblem and downloaded the copies to edge-sides. Compared with the complete resource balance situation, the additional time will accumulate to $\Delta t^{\mathrm{total}}$ after $\mathscr{L}$ steps, which will occupy more computing and communication resources of CEC architecture and adversely affect the quality of voltage control application. Therefore, the computing and communication resources of CEC architecture need to be reasonably scheduled to alleviate this situation. Based on the definition of k^{th} iteration imbalance index $H_{ib,k}$, this paper gives the allocation criteria of central processing units (denoted as the CPU clock speeds $v_{\mathrm{CPU}}^{\mathrm{cloud}}$ and $v_{\mathrm{CPU}}^{\mathrm{edge},a}$) and communication network bandwidth (denoted as the speeds of sending and receiving packets $v^{\mathrm{cl} \longrightarrow \mathrm{ed},a}$ and $v^{\mathrm{ed},a \longrightarrow \mathrm{cl}}$ between cloud-side and arbitrary edge-side a).

Furthermore, the $v_{\mathrm{CPU}}^{\mathrm{cloud}}$, $v_{\mathrm{CPU}}^{\mathrm{edge},a}$, $v^{\mathrm{cl} \longrightarrow \mathrm{ed},a}$, and $v^{\mathrm{ed} \longrightarrow \mathrm{cl},a}$ provided for ADMM can be determined by solving equations (21)–(24):

$$H_{ib,k} = \sqrt{\frac{\left(t_k^{\mathrm{cloud}} - t_k^{\mathrm{ave}}\right)^2 + \sum\limits_{a \in \mathbf{A}}\left(t_k^{\mathrm{edge},a} - t_k^{\mathrm{ave}}\right)^2}{A+1}} \le \overline{H}_{ib}, \tag{21}$$

$$t_k^{\mathrm{cloud}} = t_{\mathrm{comp},k}^{\mathrm{cloud}} + t_{\mathrm{comm},k}^{\mathrm{cl} \longrightarrow \mathrm{ed}} = \frac{\tau_{\mathrm{CPI}}^{\mathrm{cloud}} K^{\varphi} \cdot O\left(\min \varphi\left(\mathbf{x}_k\right)\right)}{v_{\mathrm{CPU}}^{\mathrm{cloud}}} + t_{\mathrm{start}}^{\mathrm{cloud}} + \max\left\{\frac{\left\|\sum_{b \in \mathbf{A}^a} \boldsymbol{\Omega}_k^{a,b}\right\|^{\mathrm{pack}} + \left\|\widehat{\mathbf{x}}_k^a\right\|^{\mathrm{pack}}}{v^{\mathrm{cl} \longrightarrow \mathrm{ed},a}}\right\} + t_{\mathrm{pack}}^{\mathrm{cloud}}, \tag{22}$$

$$t_k^{\mathrm{edge},a} = t_{\mathrm{comp},k}^{\mathrm{edge},a} + t_{\mathrm{comm},k}^{\mathrm{ed},a \longrightarrow \mathrm{cl}} = \frac{\tau_{\mathrm{CPI}}^{\mathrm{edge},a} K^{\psi} \cdot O\left(\min \psi^a\left(\mathbf{y}_k^a\right)\right)}{v_{\mathrm{CPU}}^{\mathrm{edge},a}} + t_{\mathrm{start}}^{\mathrm{edge},a} + \frac{\left\|\sum_{b \in \mathbf{A}^a} \boldsymbol{\kappa}_k^{\mathrm{ave},a,b}\right\|^{\mathrm{pack}} + \left\|\widehat{\mathbf{y}}_k^a\right\|^{\mathrm{pack}}}{v^{\mathrm{ed},a \longrightarrow \mathrm{cl}}} + t_{\mathrm{pack}}^{\mathrm{edge},a}, \tag{23}$$

$$t_k^{\mathrm{ave}} = \frac{t_k^{\mathrm{cloud}} + \sum\limits_{a \in \mathbf{A}} t_k^{\mathrm{edge},a}}{A+1}, \tag{24}$$

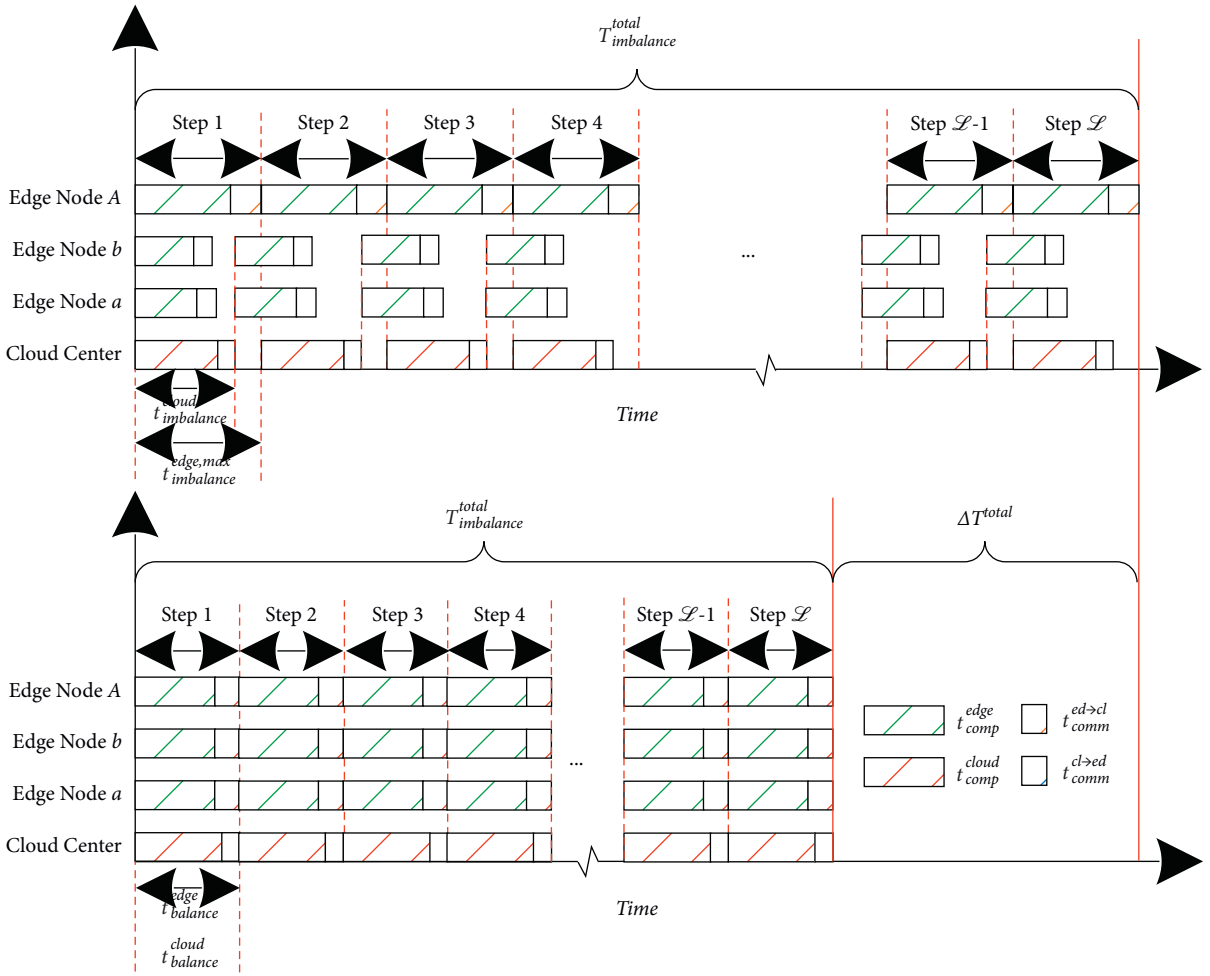

Figure 3: Influence of imbalanced resource allocation on ADMM iteration time.

where $\overline{H}_{ib}$ is the upper limit of imbalance index; $t^{\text{cloud}}_{\text{comp},k}$, $t^{\text{cl}\longrightarrow\text{ed}}_{\text{comm},k}$, and t^{cloud}_{k} are the computing, communication, and total time at cloud-side, respectively; $t^{\text{edge},a}_{\text{comp},k}$, $t^{\text{ed},a\longrightarrow cl}_{\text{comm},k}$, and $t^{\text{edge},a}_{k}$ are computing, communication, and total time at edge-side, respectively; t^{ave}_{k} is the average of t^{cloud}_{k} and all $t^{\text{edge},a}_{k}$; $O(\cdot)$ is used to the calculate time complexity; $\tau^{(\cdot)}_{\text{CPI}}$ represents the cycle per instruction; $K^{(\cdot)}$ represents the average number of instructions in single-step; $||\cdot||^{\text{pack}}$ is used to calculate the number of packets; $t^{(\cdot)}_{\text{start}}$ is the start time of ADMM single-step procedure; $t^{(\cdot)}_{\text{pack}}$ is the time of preprocessing and packaging for data frames.

Finally, the detailed steps of ADMM under CEC architecture are shown in Algorithm 2.

5. Real-Time Time-Window Stage

Note that the unexpected power fluctuations deviating from the respective scenarios may lead to voltage violations. It is required that the continuous voltage control equipment should have the real-time power regulation capabilities to maintain the bus voltages within the permitted range and guarantee the power flow boundaries satisfying $\Delta\boldsymbol{\kappa}^{a,b}_{t} = \mathbf{0}$. However, traditional localized control strategies only regulate the equipment based on local measurement information, which cannot realize the coordination among other equipment. Therefore, in this Section, a consensus-based distributed cluster control scheme is developed.

5.1. Consistency Variable Construction. Science the traditional consensus-based control methods do not consider the power flow boundary constraints, so the regulations will inevitably bring additional power flow exchange among subnetworks [33–35]. Accordingly, the power flow distribution will deviate from the optimal state. Therefore, the power flow boundary constraints are introduced into the consensus-based cluster control in this Section. Specifically, when voltage violation occurs at arbitrary bus e in the worst real-time scenarios, the ESS and PV with the highest active and reactive power regulation sensitivities will be regarded as the two leaders. The remaining ESSs and PVs are regarded as corresponding followers. By adjusting the ESS charging-discharging powers and PV inverter outputs, respectively, the voltage deviation can be kept within the allowable range under the preset boundary power flow constraint $\Delta\boldsymbol{\kappa}^{a,b}_{t} = \mathbf{0}$.

For the leaders, the consistency variables after normalization are defined as $[\mu^{a,\text{ESS}}_{\theta,t}, \mu^{a,\text{PV}}_{\omega,t}]^{\text{T}} =, [\Delta P^{\text{ESS}}_{\theta,t}/\Delta\overline{P}^{\text{ESS}}_{\theta,t}, \Delta Q^{\text{PV}}_{\omega,t}/\Delta\overline{Q}^{\text{PV}}_{\omega,t}]^{\text{T}}$, where, for ESS and PV clusters, respectively,

Initialize: $k=0$, $\varepsilon^{\text{pri}}=10^{-3}$, $\varepsilon^{\text{dual}}=10^{-3}$, $\boldsymbol{\Omega}_0=\mathbf{0}$, $\Omega_0^{a,b}=\mathbf{0}$, $\boldsymbol{\lambda}_0=\mathbf{0}$, $\lambda_0^{a,b}=\mathbf{0}$, $\rho=0.5$, $\rho^a=0.5$
[Edge-sides]: Construct representative scenarios of subnetworks
Upload representative scenarios of subnetworks to the cloud-side
[Cloud-side]: Construct representative scenarios of the whole network
Repeat
Adjust $v_{\text{CPU}}^{\text{cloud}}$ and $v_{\text{CPU}}^{\text{edge},a}$ by allocating the number of CPU cores and clock speed of each core at cloud and edge sides respectively to satisfy equation (21)
Adjust $v^{\text{cl}\longrightarrow\text{ed},a}$ and $v^{\text{ed}\longrightarrow\text{cl},a}$ by allocating uplink and downlink bandwidth of server communication port bandwidths at cloud and edge sides respectively to satisfy equation (21)
$k=k+1$
[Edge-sides]: Update $\lambda_k^{a,b}$ and $\widehat{y}_k^a$ via equations (17) and (19)
Upload $\kappa_{k-1}^{\text{ave},a,b}$, $\kappa_{k-1}^{\text{ave},b,a}$, and $\widehat{y}_k^a$ to cloud-side
[Cloud-side]: Update $\Omega_k=[\Omega_k^{a,b}]_{1\times L}$, $\boldsymbol{\lambda}_k$, and $\widehat{x}_k=[\widehat{x}_k^a]_{1\times A}$ via equations (15), (16), and (18)
Download $\Omega_k^{a,b}$ and $\widehat{x}_k^a$ to edge-sides
[Cloud-side]: Calculate R_k and S_k via equation (20)
Until $R_k\le\varepsilon^{\text{pri}}$ and $S_k\le\varepsilon^{\text{dual}}$

Algorithm 2: ADMM under CEC architecture.

the highest power sensitivity equipment is installed at bus θ and ω; $\mu_{\theta,t}^{a,\text{ESS}}$ and $\mu_{\omega,t}^{a,\text{PV}}$ are the lead consistency variables; $\Delta\overline{P}_{\theta,t}^{\text{ESS}}$ and $\Delta\overline{Q}_{\omega,t}^{\text{PV}}$ are the power change upper bounds of leaders. For the followers, the consistency variables after taking into account the sensitivity correction are defined as $[\mu_{i,t}^{a,\text{ESS}},\mu_{j,t}^{a,\text{PV}}]^{\text{T}}=[(C^PS_{ie}^P/S_{\theta e}^P)(\Delta P_{i,t}^{\text{ESS}}/\Delta\overline{P}_{i,t}^{\text{ESS}}),\quad(C^QS_{je}^Q/S_{\omega e}^Q)(\Delta Q_{j,t}^{\text{PV}}/\Delta\overline{Q}_{j,t}^{\text{PV}})]^{\text{T}}$, where $i\in\mathbf{B}^{a,\text{ESS}}$ and $i\ne\theta$; $j\in\mathbf{B}^{a,\text{PV}}$ and $j\ne\omega$; $\mu_{i,t}^{a,\text{ESS}}$ and $\mu_{j,t}^{a,\text{PV}}$ are the following consistency variables; C^P and C^Q are the active and reactive power allocation coefficients, respectively; S_{ie}^P and $S_{\theta e}^P$ are the active power sensitivity of bus i and bus θ to bus e respectively; S_{je}^Q and $S_{\omega e}^Q$ are the reactive power sensitivity of bus j and bus ω to bus e respectively; $\Delta\overline{P}_{i,t}^{\text{ESS}}$ and $\Delta\overline{Q}_{j,t}^{\text{PV}}$ are the power change upper bounds of followers. The consistency variables of leaders and followers satisfy $[\mu_{\theta,t}^{a,\text{ESS}},\mu_{\omega,t}^{a,\text{PV}}]^{\text{T}}=[\mu_{i,t}^{a,\text{ESS}},\mu_{j,t}^{a,\text{PV}}]^{\text{T}}$.

At time t, to ensure $\Delta\boldsymbol{\kappa}_t^{a,b}=0$ obtained in Section 4, as shown in Figure 4, $\boldsymbol{\kappa}_t^{a,b}$ is divided into two categories, i.e., upstream boundary $\boldsymbol{\kappa}_t^{a,\text{up}}=[U_t^{a,\text{up}},P_t^{a,\text{up}},Q_t^{a,\text{up}}]$ and downstream boundary $\boldsymbol{\kappa}_t^{a,\text{down}}=[U_t^{a,\text{down}},P_t^{a,\text{down}},Q_t^{a,\text{down}}]$. When the upstream boundary bus of arbitrary subnetwork a is regarded as slack bus, i.e., $\Delta U_t^{a,\text{up}}=0$, as long as $\Delta P_t^{a,\text{up}}=0$ and $\Delta Q_t^{a,\text{up}}=0$ as given in equation (25), there is $\boldsymbol{\kappa}_t^{a,\text{up}}=\mathbf{0}$.

$$\begin{bmatrix}\Delta P_t^{a,\text{up}}\\ \Delta Q_t^{a,\text{up}}\end{bmatrix}=\begin{bmatrix}\Delta\widetilde{P}_t^a\\ \Delta\widetilde{Q}_t^a\end{bmatrix}+\begin{bmatrix}\Delta P_{\theta,t}^{\text{ESS}}\\ \Delta Q_{\omega,t}^{\text{PV}}\end{bmatrix}+\begin{bmatrix}\sum_{i\in\mathbf{B}^{a,\text{ESS}},i\ne\theta}\Delta P_{i,t}^{\text{ESS}}\\ \sum_{j\in\mathbf{B}^{a,\text{PV}},j\ne\omega}\Delta Q_{j,t}^{\text{PV}}\end{bmatrix}=0,\tag{25}$$

where $\Delta\widetilde{P}_t^a$ and $\Delta\widetilde{Q}_t^a$ are the state variables of active and reactive power in subnetwork a respectively.

Since the downstream subnetwork of subnetwork a is adopted the same strategy, it also makes $\boldsymbol{\kappa}_t^{a,\text{down}}=\mathbf{0}$. Therefore, $\Delta\boldsymbol{\kappa}_t^{a,b}=\mathbf{0}$ is realized. Besides, before regulating, the C^P and C^Q can be determined to satisfy both $[\mu_{\theta,t}^{a,\text{ESS}},\mu_{\omega,t}^{a,\text{PV}}]^{\text{T}}=[\mu_{i,t}^{a,\text{ESS}},\mu_{j,t}^{a,\text{PV}}]^{\text{T}}$ and equation (25) only by simple algebraic calculations at the edge-side.

5.2. Consensus-Based Cluster Correction Mechanism. In the proposed consensus-based cluster correction mechanism, the leaders update power outputs in the form of droop control until the voltage amplitude of bus e returns to the allowable range. Specifically, for the k^{th} update process, the leader power outputs can be given as

$$\begin{bmatrix}\mu_{\theta,t,k}^{a,\text{ESS}}\\ \mu_{\omega,t,k}^{a,\text{PV}}\end{bmatrix}=\begin{bmatrix}\mu_{\theta,t,k-1}^{a,\text{ESS}}\\ \mu_{\omega,t,k-1}^{a,\text{PV}}\end{bmatrix}-\begin{bmatrix}\eta^P\left(U_{e,t,k-1}-\underline{\overline{U}}\right)\\ \eta^Q\left(U_{e,t,k-1}-\underline{\overline{U}}\right)\end{bmatrix},\tag{26}$$

where η^P and η^Q are used to adjust the convergence speed and accuracy of the leaders; $\underline{\overline{U}}$ represents the voltage amplitude lower limit $\underline{U}$ or upper limit $\overline{U}$.

Furthermore, the followers update their outputs according to the $k-1^{\text{th}}$ state of the leaders and adjacent followers. Considering the communication link connectivity among voltage regulation equipment, the k^{th} outputs of followers can be given as

$$\begin{bmatrix}\mu_{i,t,k}^{a,\text{ESS}}\\ \mu_{j,t,k}^{a,\text{PV}}\end{bmatrix}=\begin{bmatrix}z_{i\theta}\mu_{\theta,t,k-1}^{a,\text{ESS}}\\ z_{j\omega}\mu_{\omega,t,k-1}^{a,\text{PV}}\end{bmatrix}+\begin{bmatrix}\sum_{m\in\mathbf{B}^{a,\text{ESS}},m\ne\theta}z_{im}\mu_{m,t,k-1}^{a,\text{ESS}}\\ \sum_{n\in\mathbf{B}^{a,\text{PV}},n\ne\omega}z_{jn}\mu_{n,t,k-1}^{a,\text{PV}}\end{bmatrix},\quad\forall i\in\mathbf{B}^{a,\text{ESS}},i\ne\theta,j\in\mathbf{B}^{a,\text{PV}},j\ne\omega,\tag{27}$$

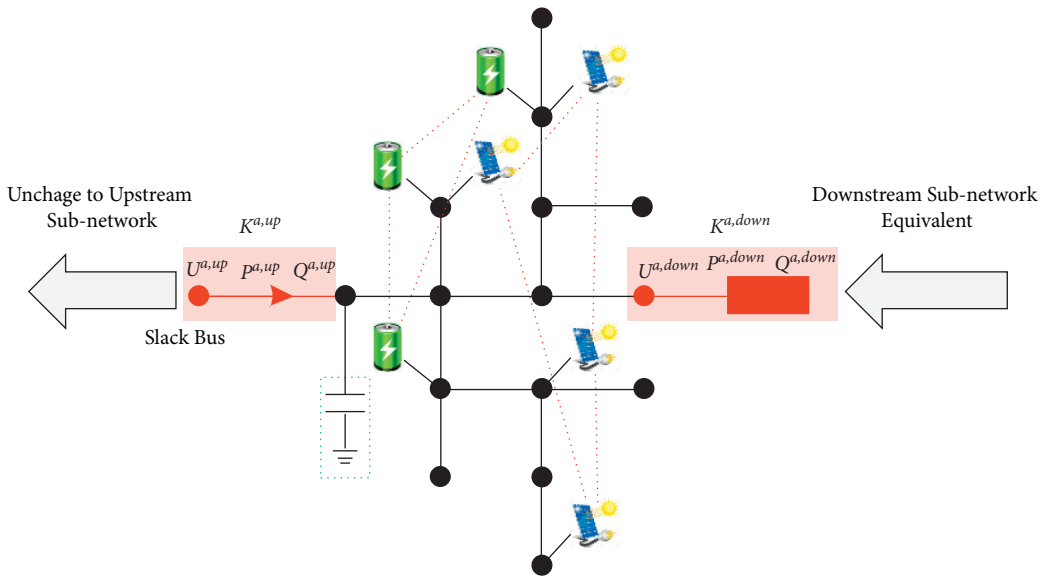

Figure 4: Strategy to realize $\Delta\boldsymbol{\kappa}_t^{a,b} = \mathbf{0}$.

where $z_{\sigma\delta}$ ($\sigma = i$ or j; $\delta = \theta$, ω, m, or n) represents the state transition coefficient, generally determined by the means Metropolis algorithm [33]:

$$z_{\sigma\delta} = \begin{cases} \dfrac{2}{1 + d_\sigma + d_\delta}, & \sigma\delta \in \boldsymbol{\Theta}_\sigma^{a,\mathrm{ESS/PV}}, \\ 1 - \displaystyle\sum_{\sigma\delta \in \boldsymbol{\Theta}_\sigma^{a,\mathrm{ESS/PV}}} \dfrac{2}{1 + d_\sigma + d_\delta}, & j = i, \\ 0, & \text{otherwise}, \end{cases} \tag{28}$$

where $\Theta_\sigma^{a,\mathrm{ESS/PV}}$ σ represents the set of links that have a direct communication connection with ESS or PV installed at bus σ; d_σ and d_δ represent the point connectivities of bus σ and δ respectively, i.e., the number of equipment with direct communication links to ESS or PV installed at bus σ and δ.

Finally, the detailed steps of the proposed consensus-based cluster correction mechanism are shown in Algorithm 3.

6. Case Studies

In this Section, improved 33-bus and IEEE 123-bus systems are used to test the effectiveness of our proposed CEC-DCVC method. The centralized stochastic programming method proposed in [8], the decentralized stochastic programming method proposed in [21], and the CEC robust optimization method are adopted as the comparisons.

The software and hardware adopted in the simulations are as follows. The cloud server adopts Intel Xeon 4 CPU@ 3.2GHz, 8 GB RAM with Win 10, while edge servers adopt Intel Core i5 CPU@2.4GHz, 4 GB RAM with Win 10. 100 Mbps communication links with TCP protocol are adopted to exchange copies among cloud-side control center and edge computing devices, while 10 Mbps communication links with UPD protocol are adopted to realize consensus-based cluster control among the continuous voltage control equipment. The CEC architecture is implemented on the Microsoft Visual Studio 2019 platform based on multiagent technology. GUROBI 8.9.0 in MATLAB 2018b is adopted to solve the ADMM subproblems.

6.1. Voltage Control Results of Modified 33-Bus System

6.1.1. Modified 33-Bus System. The 33-bus system [36] with three subnetworks is firstly tested, as shown in Figure 5. The allowed operational voltage range $[\underline{U}, \overline{U}] = [0.95, 1.05]$ p.u. The parameters of voltage control equipment are demonstrated in Table 1. The maximal allowable hourly and daily action limits of the OLTC are 4 and 30 times, respectively, and action limits of CBs are 2 and 15 times, respectively. Without losing generality, we assume that ESSs are distributed near PVs, and PVs in each subnetwork have the same generation. In addition, we assume that all load buses have the same power demand factor, which represents the ratio of forecasting load demand magnitudes to the reference operating magnitudes, as shown in Figure 6.

6.1.2. Results in the Interval Dispatch Stage. The forecasting curves described in Figure 6 are used as the probability distribution means for stochastic programming. In addition, assume that the load demands obey the Gauss distribution with 5% standard deviations, while the PV outputs obey the Beta distribution, where both two shape parameters are set as 6.06. Then, 100 representative scenarios are generated by using the proposed method in Section 4.1.3. For example, Figure 7 shows the possible voltage amplitudes at 12 : 00. It can be seen that about 10% of representative scenarios show bus voltage violations, with the maximum voltage of 1.067 p.u. Therefore, it is necessary to carry out voltage control.

Initialize: $k = 0$, $\eta^P = 1$, $\eta^Q = 1$
[Edge-side]: Marking bus θ and bus ω with the highest active and reactive sensitivity equipment to voltage violation bus e
[Edge-side]: Calculate C^P and C^Q to satisfy $[\mu_{\theta,t}^{a,\mathrm{ESS}}, \mu_{\omega,t}^{a,\mathrm{PV}}]^{\mathrm{T}} = [\mu_{i,t}^{a,\mathrm{ESS}}, \mu_{j,t}^{a,\mathrm{PV}}]^{\mathrm{T}}$ and equation (25)
Repeat
$k = k + 1$
If $U_{e,t,k} > \overline{U}$ or $U_{e,t,k} < \underline{U}$
[ESS & PV leaders]: Update $\mu_{\theta,t}^{a,\mathrm{ESS}}$ and $\mu_{\omega,t}^{a,\mathrm{PV}}$ via equation (26)
Else
[ESS & PV leaders]: Maintain $\mu_{\theta,t}^{a,\mathrm{ESS}}$ and $\mu_{\omega,t}^{a,\mathrm{PV}}$
[ESS & PV followers]: Update $\mu_{i,t,k}^{a,\mathrm{ESS}}$ and $\mu_{j,t,k}^{a,\mathrm{PV}}$ via equation (27)
Until $\max\left\{\mu_{i,t,k}^{a,\mathrm{ESS}}, \mu_{j,t,k}^{a,\mathrm{PV}}\right\} \leq 10^{-2}$.

Algorithm 3: Consensus-based cluster correction mechanism.

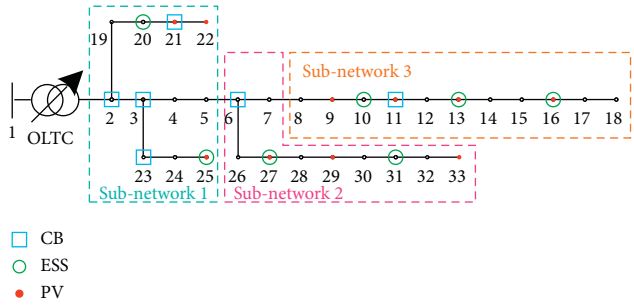

Figure 5: Modified 33-bus system.

Table 1: Parameters of OLTC, CBs, PVs, and ESSs.

Voltage control equipment	Types	Subnetworks	Parameters	Placement buses
Discrete equipment	OLTC	—	0.005 p.u/tap ∗ 20 taps	1
	CB	1, 2, 3	30 kVar/tap ∗ 10 taps	2, 3, 6, 11, 21, 23
Continuous equipment	PV1	1	450 kVA	21, 22, 25
	PV2	2	450 kVA	27, 29, 33
	PV3	3	500 kVA	9, 11, 13, 16
	ESS1	1	500 kWh	20, 25
	ESS2	2	600 kWh	27, 31
	ESS3	3	600 kWh	10, 13, 16

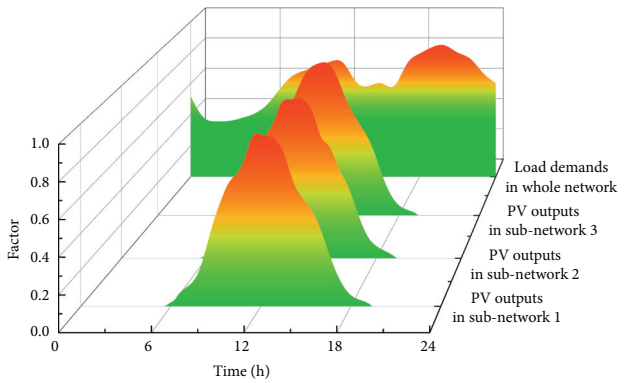

Figure 6: Forecasting curves of PV active power output and load demand factors.

The hourly tap positions of OLTC and CBs within one day determined by conducting the proposed cloud-side ADMM algorithm are shown in Figure 8. The 15 min reference reactive power outputs of PVs and charging-discharging curves of ESSs determined by conducting the edge-side ADMM algorithms are shown in Figure 9.

Under the CEC architecture, the proposed DCVC method can realize the coordination of discrete and continuous types of equipment with different timescales. According to Figure 8, to guarantee the hourly global optimal power flows, the taps of OLTC over the day change 22 times, while the average taps of CBs are 3.465. Furthermore, as shown in Figure 9, there exists a significant difference in the continuous equipment power outputs in the daytime and night:

(i) In the daytime, the average ESS charging power is 38.79 kW, 45.73 kW, and 53.45 kW in subnetworks 1, 2, and 3 to absorb the additional active power output of PVs. The average PV inverter reactive power outputs are 59.43 kVar, 213 kVar, and −32 kVar in subnetworks 1, 2, and 3. Especially, when PV active power outputs reach the peaks, the

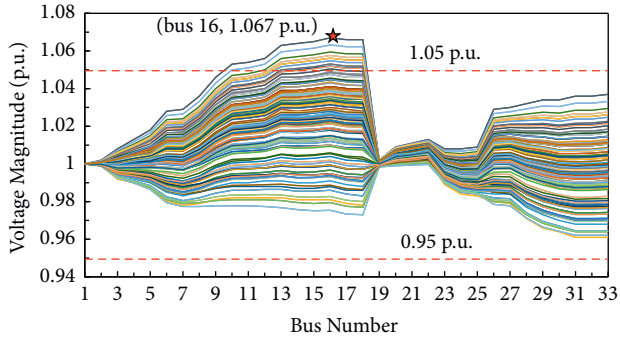

Figure 7: Voltage magnitudes at 12 : 00 under representative scenarios without control.

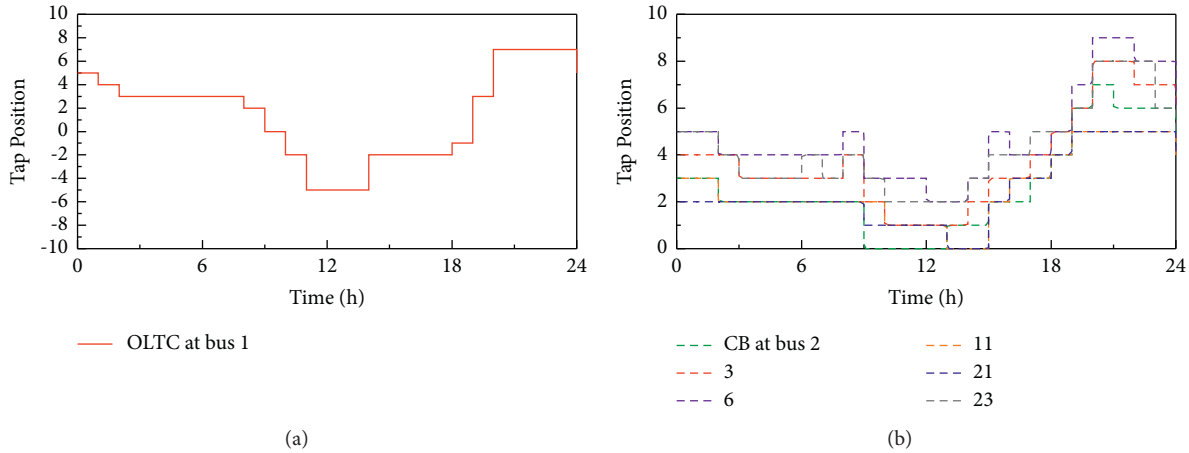

Figure 8: Hourly tap positions for 33-bus system. (a) OLTC. (b) CBs.

PV reactive outputs are close to 0 or even negative to absorb the inductive reactive powers from the distribution network to reduce the bus voltage amplitudes. Conversely, when PV active outputs are at low levels, the PV inverters increase their reactive power outputs to raise the bus voltage amplitudes.

(ii) In the night, the average ESS discharge power is 22.16 kW, 36.45 kW, and 43.29 kW in subnetworks 1, 2, and 3, respectively, to support high load demands. Since the PV active power outputs are close to 0, the PV inverter reactive power outputs are increased to support the bus voltage. In this case, the average PV reactive power outputs are 77.58 kVar, 287 kVar, and 111.34 kVar in subnetworks 1, 2, and 3, respectively. Finally, in this test system, the voltage qualification rate is 100% under representative scenarios, while the average bus voltage deviation is 0.0121 p.u. and the power loss is 45.23 kW.

6.1.3. Results in the Real-Time Time-Window Stage. In this stage, 5000 random scenarios are generated by the Monte Carlo sampling method to simulate the uncertain PV active power outputs and load demands deviating from the representative scenarios. By using the proposed consensus-based cluster correction strategy in Section 5, the correction results of bus 16 with the largest voltage deviations under the worst real-time scenarios are shown in Figure 10.

Under the worst real-time scenarios from 10 : 25 : 00 to 12 : 45 : 00, the voltage amplitude of bus 16 exceeds the lower limit 5 times. The maximum voltage deviation occurs at 10 : 25 : 00 with the lowest voltage magnitude 0.937 p.u. The possible reason causing such a sharp drop may be the sudden power drops of PVs at the high-level load demands. In this case, by precomputing the sensitivity matrix, the ESS and PV installed at bus 16 are determined as the active and reactive power regulation leaders, respectively, while the ESSs and PV at buses 9, 10, 11, and 13 are regarded as the followers. Under the optimal power flow boundary constraints obtained by the proposed ADMM algorithm, the regulation processes with the proposed consensus-based cluster correction strategy are shown in Figure 11.

Figures 11(a) and 11(b) illustrate that the states of ESSs and PV inverters reach the consensuses after 45 and 51 iterations, respectively. The maximum deviations during the regulation process are 1.01% and 2.73%, respectively. The corresponding boundary power flow fluctuations are presented in Figure 12. Since the PV outputs in subnetwork 3 have been greatly reduced, the $P_t^{3,\mathrm{up}}$ is suddenly increased by 0.198 MW. But with the ESS consensus-based cluster correction process, the optimal active power boundary can be

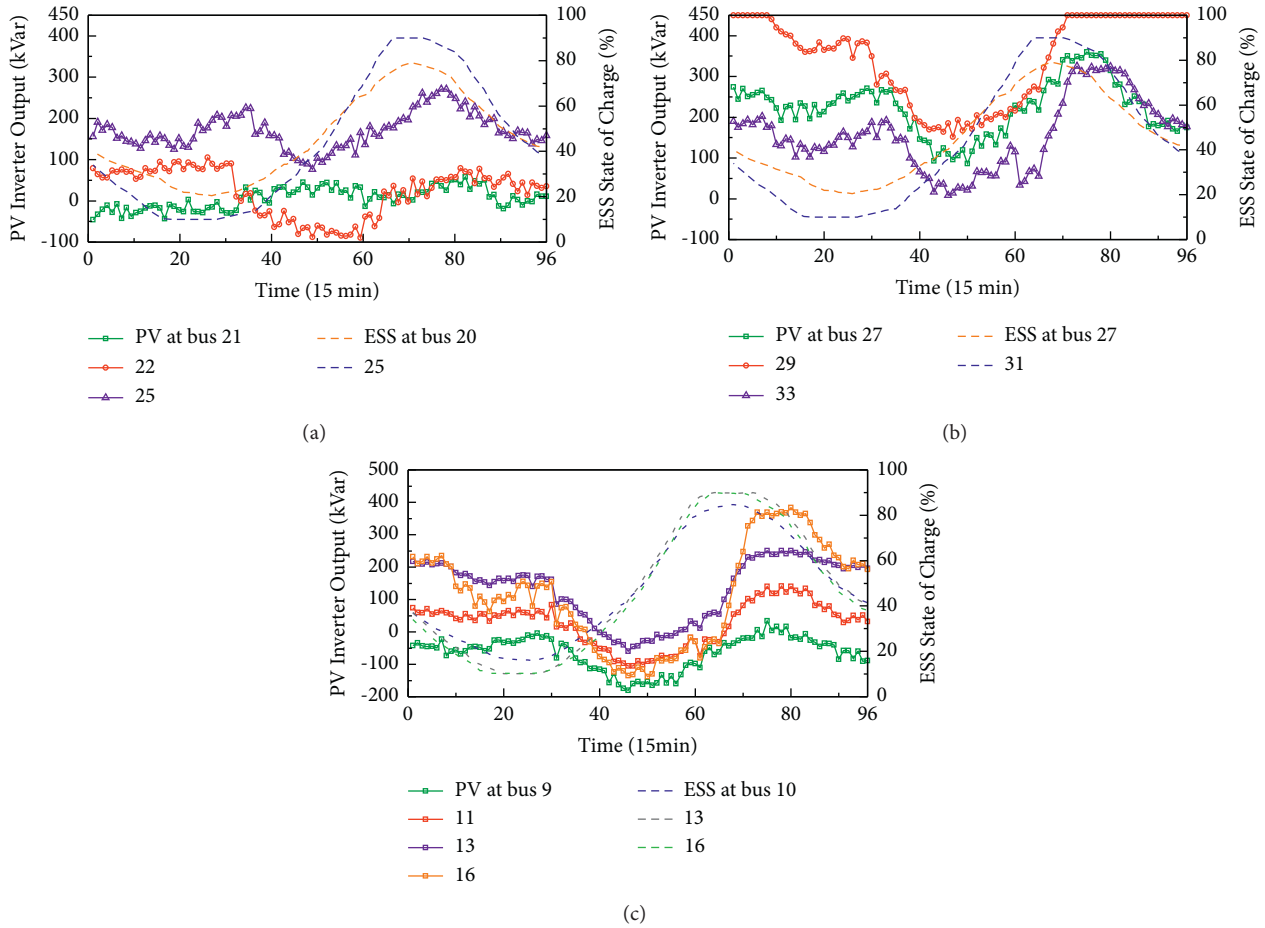

Figure 9: 15 min PV inverter reference outputs and ESS states of charge for 33-bus system. (a) Subnetwork 1. (b) Subnetwork 2. (c) Subnetwork 3.

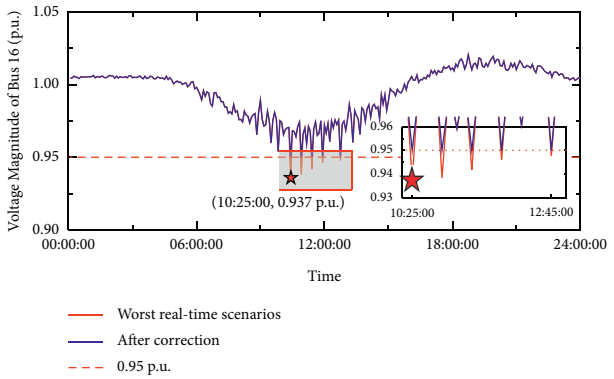

Figure 10: Correction results of bus 16 under the worst real-time scenarios.

restored within 0.84 s. Meanwhile, the PV leader increases the reactive power output, so that the PV followers need to reduce their reactive power outputs to balance $Q_t^{3,\mathrm{up}}$. The overall time-consuming is only 1.10 s, and the maximum reactive power fluctuation is 0.014 MVar, which satisfies the real-time control requirements. Besides, the correction process in this stage only occurs in subnetwork 3, which has no impact on the optimal operation of other subnetworks.

6.2. Voltage Control Results of Modified IEEE 123-Bus System

6.2.1. Modified IEEE 123-Bus System. As shown in Figure 13, the IEEE 123-bus system [37] with three subnetworks is tested to verify the effectiveness of our proposed method under larger-scale distribution networks. The load demand curves and discrete equipment parameters for this system are the same as the 33-bus system. OLTC is installed at bus 1. CBs are installed at buses {19, 28, 43, 63, 80, 91, 106, 118}. The PV output curves and continuous equipment parameters in the subnetworks 1, 2, and 3 are the same as those in the subnetworks of the 33-bus system, while the assumptions of subnetwork 3 in 33-bus system are adopted in subnetwork 4 here. ESSs and PVs are located at buses {15, 20, 27, 39, 45, 53, 56, 74, 78, 82, 87, 98, 113} and {14, 18, 21, 26, 31, 35, 46, 49, 57, 65, 68, 74, 77, 78, 85, 90, 93, 98, 113}, respectively.

6.2.2. Results in the Interval Dispatch Stage. Due to the increased number and scale of subnetworks, the operating conditions in subnetworks are more complex. Thereby, the number of representative scenarios increases to 200. However, the proposed DCVC method can still coordinate the discrete and continuous types of equipment under CEC

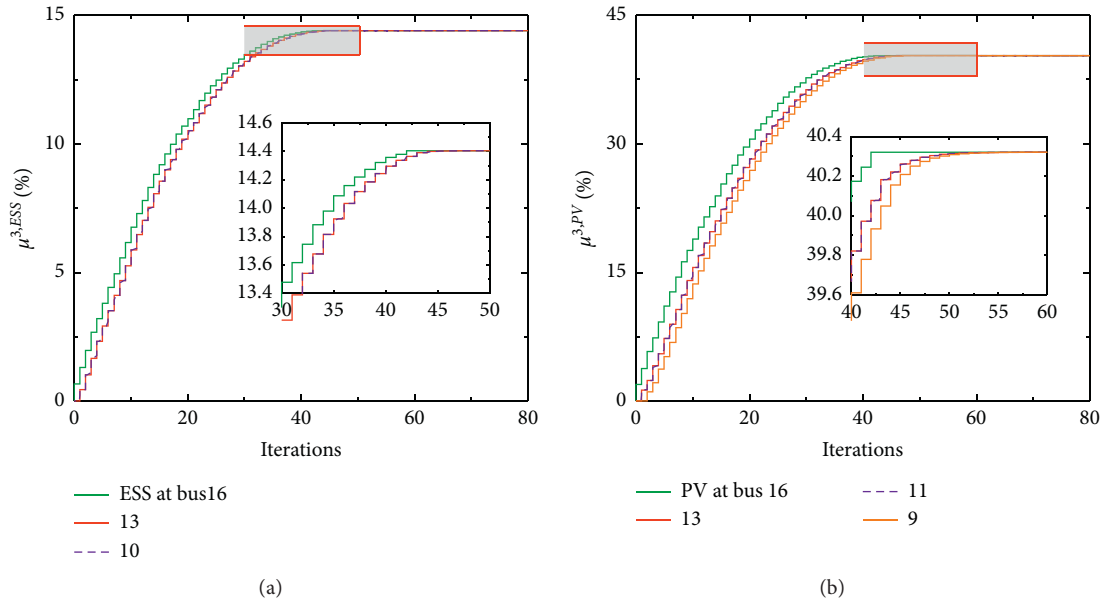

Figure 11: Iterative processes of consensus-based cluster correction in subnetwork 3 of 33-bus system. (a) ESS cluster. (b) PV cluster.

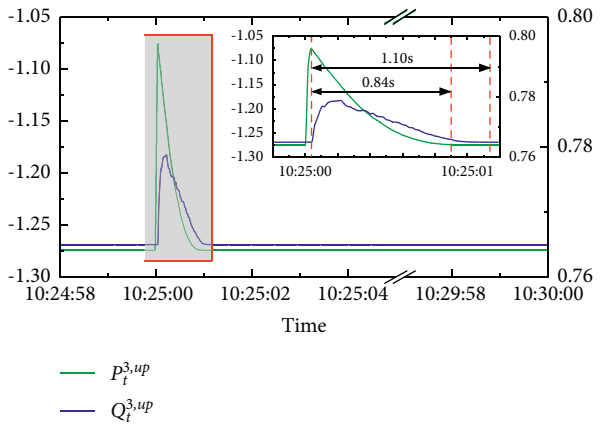

Figure 12: Boundary power flow fluctuations during consensus-based cluster correction.

architecture, as shown in Table 2. Finally, in this test system, the voltage qualification rate can also be maintained at 100%, while the average voltage deviation is 0.0137 p.u. and the power loss is 124.23 kW.

6.2.3. Results in the Real-Time Time-Window Stage. Without losing generality, bus 2 with the most serious voltage violation under the worst scenario is taken as an example for discussion and analysis. As shown in Figures 14(a) and 14(b), although the number of ESS and PV increases to 4 and 6, respectively, both the ESS and PV cluster consistency variables can still well converge within the allowed time. Specifically, the two equipment clusters converge after 66 and 88 iterations, respectively. The corresponding time-consumption is 1.23 s and 1.58 s, respectively. In addition, the maximum deviations of two consistency variables are limited to 5%.

6.3. Comparison with Current Methods. To verify the superior control performance of the proposed CEC-DCVC method in multitimescale, the following five methods are compared:

(1) Method #1: with no control method

(2) Method #2: with the proposed CEC-DCVC method

(3) Method #3: with the centralized stochastic programming method in [8]

(4) Method #4: with the decentralized stochastic programming method in [21]

(5) Method #5: with the CEC robust optimization method

During one day, the average voltage deviation $|\Delta U|$ of each bus is shown in Figure 15. The control results of subnetworks and the whole network are shown in Tables 3 and 4.

The results indicate that the proposed method #2 has a better performance than others in reducing voltage deviations and power losses. Specifically, although method #3 has a similar power loss reduction performance in the two test systems compared with our proposed method #2, the average voltage deviations with method #3 are 16.67% and 19.90% larger, respectively. This is because method #3 only focused on minimizing the power losses without considering the voltage deviations. In addition, because the centralized control structure is used in method #3, only one representative scenario set is adopted during determining the optimal power flows. Conversely, in our proposed method #2, not only both the voltage deviations and power losses are considered as the optimization objectives, more fine representative scenario sets considering the differences among the subnetworks are established in our paper as well. Moreover, since method #4 fails to avoid the interregional suboptimal power flows

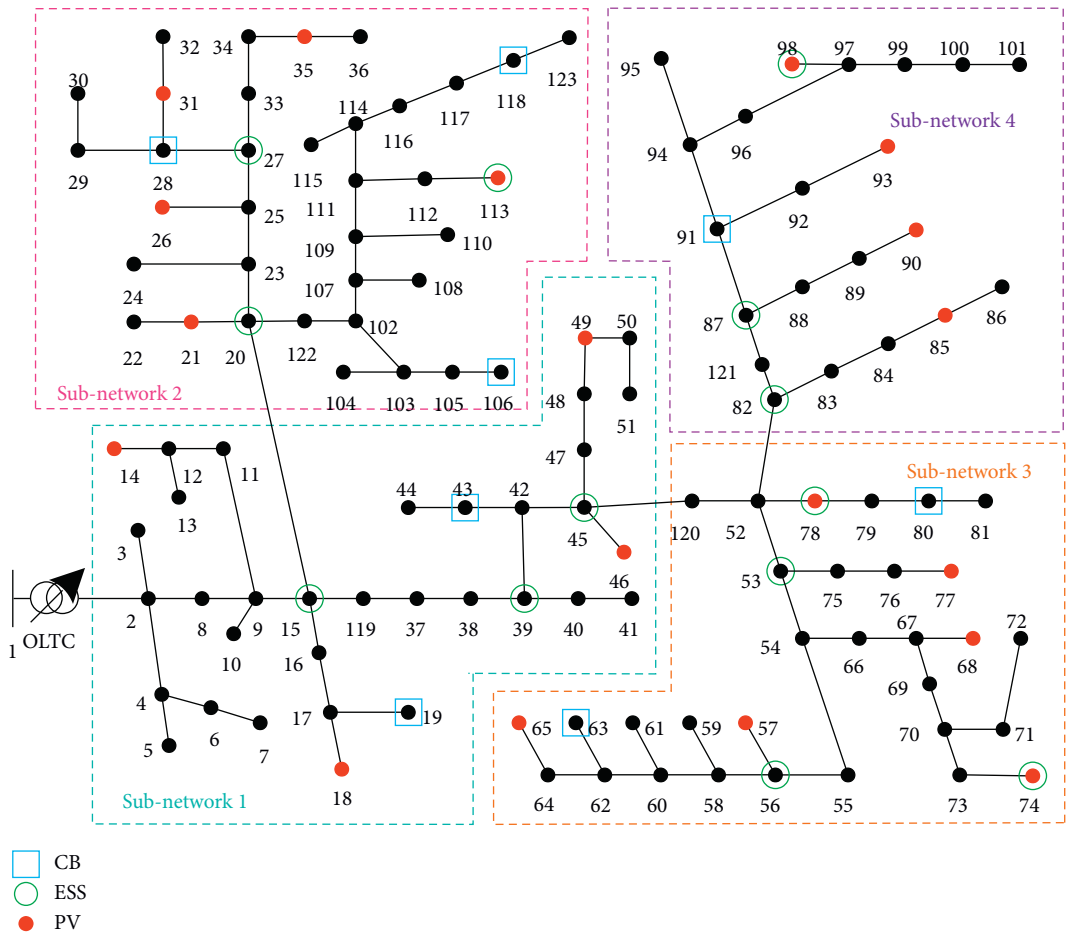

Figure 13: Modified IEEE 123-bus system.

Table 2: Voltage control equipment operation conditions in the interval dispatch stage of IEEE 123-bus system.

Interval dispatch elements		Operation conditions
Changing taps of OLTC		24
Average taps of CBs		4.35
Average output of PV inverters in day/night (kVar)	Subnetwork 1	34.26/134.21
	Subnetwork 2	−52.38/206.42
	Subnetwork 3	−123.62/234.34
	Subnetwork 4	−69.46/269.15
Average charge/discharge power of ESSs (kW)	Subnetwork 1	35.46/19.14
	Subnetwork 2	41.47/32.25
	Subnetwork 3	53.36/42.42
	Subnetwork 4	43.82/31.71

during partial localized voltage control, the average voltage deviations in the two test systems are increased by 4.21% and 7.19%, respectively, while the power losses are increased by 5.14% and 6.98% compared with our proposed method #2. In addition, although method #5 adopts the same CEC architecture as our proposed method #2, the average voltage deviations in the two test systems are increased by 32.63% and 19.25%, respectively, while the power losses are increased by 23.53% and 24.24% compared with our proposed method #2. The reason is that the conservative results under the worst scenarios are usually obtained in robust method #5.

6.4. Resource Balance Performance. To be more practical, assume that the CEC architecture also undertakes some other applications except for voltage control, such as power scheduling [29], stability operation control [30], and load forecasting [31]. When the voltage control application and those other applications overlap during the solving process, heterogeneous and limited computing resources will be provided to the voltage control application. Without losing generality, in this section, the benchmark utilization of CPU and bandwidth is set as an overload situation [38] to simulate the above situation under CEC architecture. As shown in Figures 16(a) and 16(b), under the traditional polling

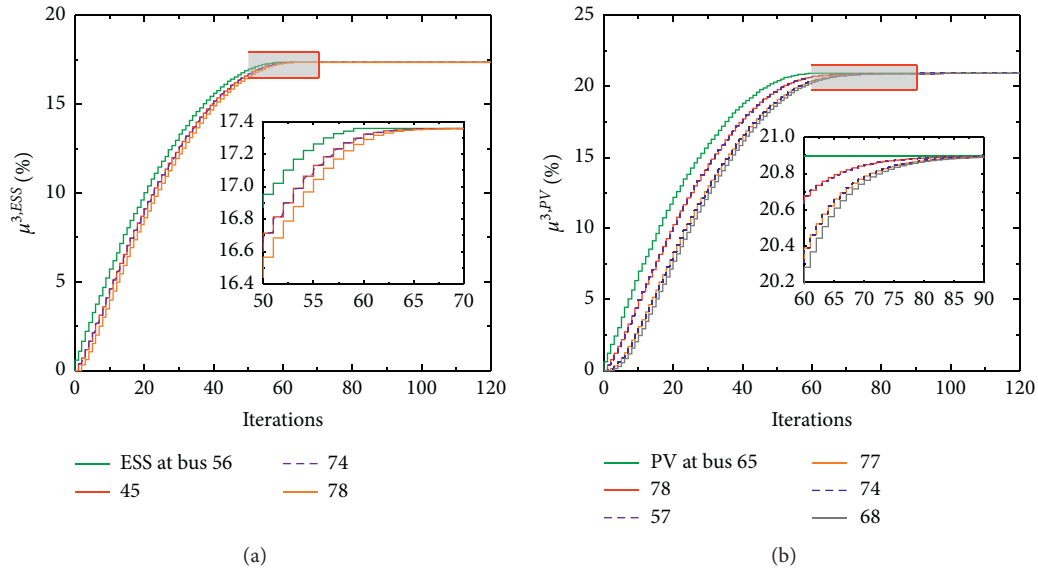

Figure 14: Iterative processes of consensus-based cluster corrections in subnetwork 3 of IEEE 123-bus system. (a) ESS cluster. (b) PV cluster.

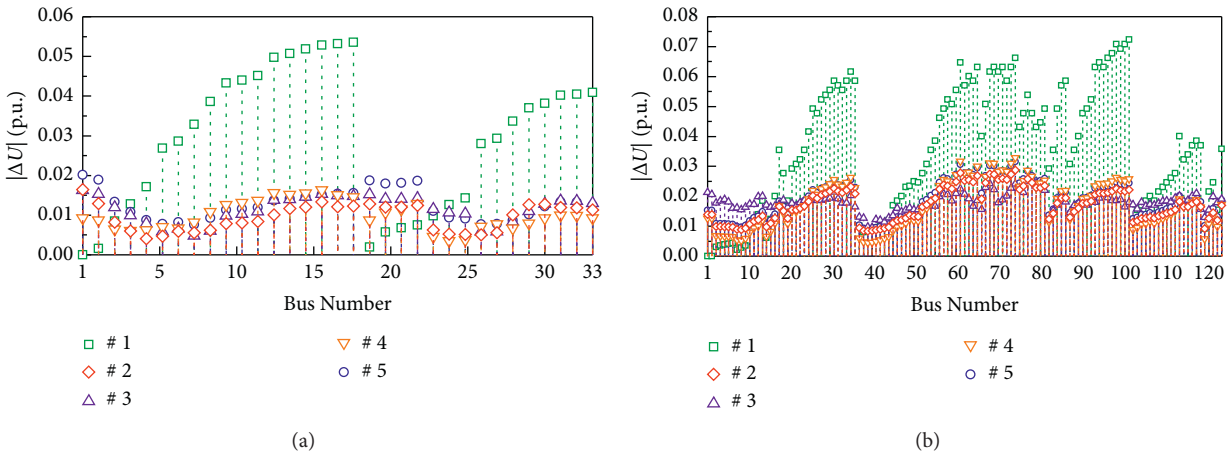

Figure 15: Average voltage deviation $|\Delta U|$ of each bus. (a) 33-bus system. (b) IEEE 123-bus system.

Table 3: Control results of five methods in 33-bus system.

Method		#1	#2	#3	#4	#5
Average $\|\Delta U\|$ (p.u.)	Subnetwork 1	0.0090	0.0088	0.0123	0.0076	0.0141
	Subnetwork 2	0.0343	0.0092	0.0096	0.0082	0.0101
	Subnetwork 3	0.0469	0.0098	0.0117	0.0137	0.0128
	Whole network	0.0290	0.0095	0.0114	0.0099	0.0126
Power loss (kW)	Whole network	124.67	48.83	48.96	51.34	58.23

Table 4: Control results of five methods in IEEE 123-bus system.

Method		#1	#2	#3	#4	#5
Average $\|\Delta U\|$ (p.u.)	Subnetwork 1	0.0121	0.0122	0.0158	0.0080	0.0121
	Subnetwork 2	0.0359	0.0163	0.0183	0.0162	0.0185
	Subnetwork 3	0.0506	0.0172	0.0205	0.0240	0.0258
	Subnetwork 4	0.0532	0.0163	0.0177	0.0194	0.0204
	Whole network	0.0358	0.0153	0.0191	0.0164	0.0189
Power loss (kW)	Whole network	354.41	132.12	132.71	141.34	164.15

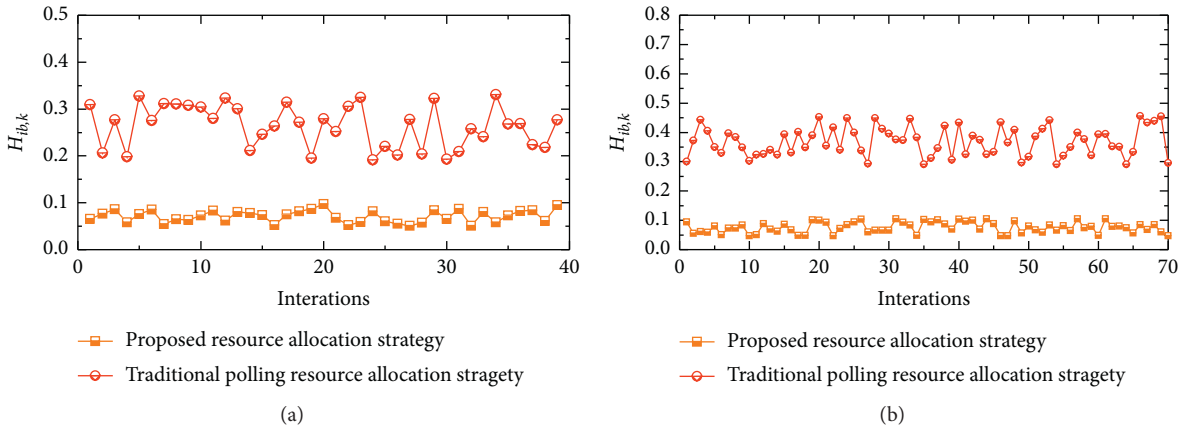

FIGURE 16: Imbalance indexes $H_{ib,k}$ during the iterative processes. (a) 33-bus system. (b) IEEE 123-bus system.

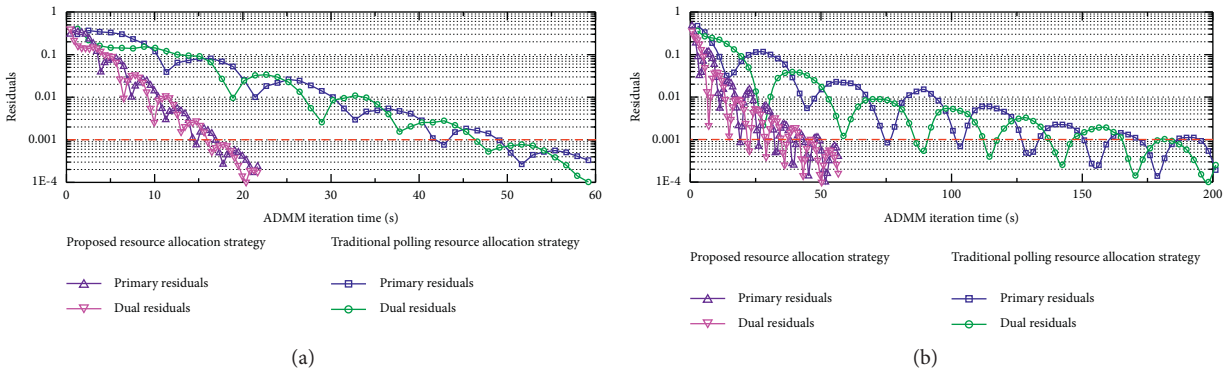

FIGURE 17: Iterative process of ADMM. (a) 33-bus system. (b) IEEE 123-bus system.

resource allocation strategy [39], the average resource allocation imbalance indexes $H_{ib,k}$ are 0.264 and 0.374, respectively, for two test systems during the iterative processes. As shown in Figures 17(a) and 17(b), the corresponding total solving time-consumption reaches 49.12 s and 195.93 s, which exacerbate the high computing pressure duration under CEC architecture in multiapplication cases. In addition, overlong solving time-consumption is adverse to meet the correspondence between the control strategies and the actual working conditions. After executing the proposed computing and communication resource allocation strategy, the average resource allocation imbalance indexes $H_{ib,k}$ are greatly reduced to 0.071 and 0.075, respectively. The corresponding total solution time is decreased to 16.91 s and 49.59 s. Besides, as demonstrated in Figures 17(a) and 17(b), different resource allocation strategies do not affect the iterations required for ADMM convergence, where two test systems converge after 39 and 70 iterations.

7. Conclusion

To solve the multitimescale voltage control problem of high PV-penetrated distribution networks, this paper proposes a CEC-DCVC method, which decomposes the global voltage control task and solves it coordinately. It effectively reduces the voltage deviations and power losses and realizes an excellent allocation of computing and communication resources. Compared with the centralized method, the model dimensions and algorithm time complexity are greatly reduced. Besides, its scalability is significantly improved, suitable for photovoltaic frequent fluctuation scenarios. Compared with the decentralized method, due to the introduction of optimal power flow boundary constraints, unnecessary power interactions among subnetworks during local voltage regulations are avoided. Furthermore, the complete decoupling of voltage regulations in each subnetwork is realized. Besides, the cloud-side control center is used to undertake the partial optimization model, which effectively reduces the computing burden on edge-side devices with limited computing and communication resources.

Moreover, the proposed method is a general method based on optimal power flow stochastic programming, which can be extended to other applications based on the CEC architecture in distribution networks.

Appendix

A.1. Constraints at the Cloud-Side

A.1. Power Flow Constraints of Second-Order Cone Form for Whole Network.

$$\sum_{k\in\boldsymbol{\eta}(j)} P_{jk,t} - \sum_{i\in\boldsymbol{\gamma}(j)} \left(P_{ij,t} - l_{ij,t}r_{ij}\right) = P_{j,t}^{\mathrm{PV}} + \widehat{P}_{j,t}^{\mathrm{ESS}} - P_{j,t}^{\mathrm{load}}, \tag{A.1}$$

$$\sum_{k\in\boldsymbol{\eta}(j)} Q_{jk,t} - \sum_{i\in\boldsymbol{\gamma}(j)} \left(Q_{ij,t} - l_{ij,t}x_{ij}\right) = Q_{j,t}^{\mathrm{CB}} + \widehat{Q}_{j,t}^{\mathrm{PV}} - Q_{j,t}^{\mathrm{load}}, \tag{A.2}$$

$$u_{j,t} = u_{i,t} + \left(r_{ij}^2 + x_{ij}^2\right)l_{ij,t} - 2\left(r_{ij}P_{ij,t} + x_{ij}Q_{ij,t}\right), \tag{A.3}$$

$$\left\| \begin{matrix} 2P_{ij,t} \\ 2Q_{ij,t} \\ l_{ij,t} - u_{j,t} \end{matrix} \right\|_2 \le l_{ij,t} + u_{j,t}. \tag{A.4}$$

(A.1)-(A.4), $\forall ij \in \mathbf{E}, j \in \mathbf{B}$, where $\mathbf{B}$ is the bus set of the whole network; x_{ij} represents the reactance of branch ij; $\boldsymbol{\eta}(j)$ and $\boldsymbol{\gamma}(j)$ are the sets of power injection and outflow at bus j respectively; $P_{j,t}^{\mathrm{PV}}$ is the active power output of PV at bus j; $\widehat{P}_{j,t}^{\mathrm{ESS}}$ and $\widehat{Q}_{j,t}^{\mathrm{PV}}$ are the copies of ESS discharge power and PV inverter reactive power output respectively; $P_{ij,t}$ represents the active power of branch ij; $Q_{j,t}^{\mathrm{CB}}$ is the reactive power compensation of CB; and $Q_{j,t}^{\mathrm{load}}$ is the reactive power of load demand.

A.2. OLTC Constraints.

$$\alpha_{m,t} \in \{0,1\}, \quad \forall m \in \mathbf{M}, \tag{A.5}$$

$$\sum_{m\in\mathbf{M}} \alpha_{m,t} = 1, \tag{A.6}$$

$$u_{1,t} = \sum_{m\in\mathbf{M}} \left(U_0 + U^{\mathrm{tap}}k_m\right)^2 \alpha_{m,t}, \tag{A.7}$$

$$\left| \sum_{m\in\mathbf{M}} k_m\alpha_{m,t} - \sum_{m\in\mathbf{M}} k_m\alpha_{m,t-\Delta t} \right| \le \overline{K}_t^{\mathrm{OLTC}}, \tag{A.8}$$

$$\sum_{t\in\mathbf{T}^{\mathrm{cloud}}} \left| \sum_{m\in\mathbf{M}} k_m\alpha_{m,t} - \sum_{m\in\mathbf{M}} k_m\alpha_{m,t-\Delta t} \right| \le \overline{K}^{\mathrm{OLTC}}, \tag{A.9}$$

where $\alpha_{m,t}$ is the virtual binary variable, which represents the state of OLTC; $\mathbf{M}$ is the tap set of OLTC; U^{tap} is the voltage particle size of each tap; k_m represents OLTC in the m^{th} tap; $\overline{K}_t^{\mathrm{OLTC}}$ and $\overline{K}^{\mathrm{OLTC}}$ are the hourly and daily limit of changing taps for OLTC, respectively.

A.3. CB Constraints

$$\beta_{j,n,t} \in \{0,1\}, n \in \mathbf{N}, \tag{A.10}$$

$$Q_{j,t}^{\mathrm{CB}} = Q_0^{\mathrm{CB}} \sum_{n\in\mathbf{N}} \beta_{j,n,t}, \tag{A.11}$$

$$\left| \sum_{n\in\mathbf{N}} \beta_{j,n,t} - \sum_{n\in\mathrm{N}} \beta_{j,n,t-\Delta t} \right| \le \overline{K}_t^{\mathrm{CB}}, \tag{A.12}$$

$$\sum_{t\in\mathbf{T}^{\mathrm{cloud}}} \left| \sum_{n\in\mathbf{N}} \beta_{j,n,t} - \sum_{n\in\mathrm{N}} \beta_{j,n,t-\Delta t} \right| \le \overline{K}^{\mathrm{CB}}. \tag{A.13}$$

(A.10)-(A.13), $\forall j \in \mathbf{B}^{\mathrm{CB}}$, where $\beta_{j,n,t}$ is the virtual binary variable, which represents the state of CB at bus j; $\mathbf{B}^{\mathrm{CB}}$ is the set of CBs; $\mathbf{N}$ is the tap set of CB; Q_0^{CB} represents the capacity of each tap for CB; $\overline{K}_t^{\mathrm{CB}}$ and $\overline{K}^{\mathrm{CB}}$ are the hourly and daily limit of changing taps for CBs, respectively.

B. Constraints at the Edge-Sides

B.1. Power Flow Constraints of Second-Order Cone Form for Subnetworks.

$$\sum_{k\in\boldsymbol{\eta}(j)} P_{jk,t} - \sum_{i\in\boldsymbol{\gamma}(j)} \left(P_{ij,t} - l_{ij,t}r_{ij}\right) = P_{j,t}^{\mathrm{PV}} + P_{j,t}^{\mathrm{ESS}} - P_{j,t}^{\mathrm{load}}, \tag{B.1}$$

$$\sum_{k\in\boldsymbol{\eta}(j)} Q_{jk,t} - \sum_{i\in\boldsymbol{\gamma}(j)} \left(Q_{ij,t} - l_{ij,t}x_{ij}\right) = \widehat{Q}_{j,t}^{\mathrm{CB}} + Q_{j,t}^{\mathrm{PV}} - Q_{j,t}^{\mathrm{load}}, \tag{B.2}$$

$$u_{j,t} = u_{i,t} + \left(r_{ij}^2 + x_{ij}^2\right)l_{ij,t} - 2\left(r_{ij}P_{ij,t} + x_{ij}Q_{ij,t}\right), \tag{B.3}$$

$$\left\| \begin{matrix} 2P_{ij,t} \\ 2Q_{ij,t} \\ l_{ij,t} - u_{j,t} \end{matrix} \right\|_2 \le l_{ij,t} + u_{j,t}, \tag{B.4}$$

$$\left(\underline{U}\right)^2 \le u_{j,t} \le \left(\overline{U}\right)^2, \tag{B.5}$$

$$0 \le l_{ij,t} \le \left(\overline{I}\right)^2. \tag{B.6}$$

(B.1)-(B.6), $\forall ij \in \mathbf{E}^a, j \in \mathbf{B}^a, t \in \mathbf{T}^{\mathrm{edge}}, a \in \mathbf{A}$, where $\underline{U}$ and $\overline{U}$ are the lower and upper limit of buses voltage, respectively; $\widehat{Q}_{j,t}^{\mathrm{CB}}$ is the copy form of reactive power compensation for CB; and $\overline{I}$ represents the upper limit of branches current.

B.2. ESSs Constraints

$$-\overline{P}_j^{\mathrm{ESS}} \le P_{j,t}^{\mathrm{ESS}} \le \overline{P}_j^{\mathrm{ESS}}, \tag{B.7}$$

$$P_{j,t}^{\mathrm{ESS}} = \frac{E_j^{\mathrm{ESS}}\left(S_{j,t+\Delta t'}^{\mathrm{oC}} - S_{j,t}^{\mathrm{oC}}\right)}{\Delta t'}, \tag{B.8}$$

$$\underline{S}_j^{\mathrm{oC}} \le S_{j,t}^{\mathrm{oC}} \le \overline{S}_j^{\mathrm{oC}}. \tag{B.9}$$

(B.7)-(B.9), $\forall j \in \mathbf{B}^{a,\mathrm{ESS}}$, where E_j^{ESS} is the capacity of ESS installed at bus j; $\overline{P}_j^{\mathrm{ESS}}$ represents the limit of discharge power rate; $\underline{S}_j^{\mathrm{oC}}$ and $\overline{S}_j^{\mathrm{oC}}$ are the lower and upper limits of ESS states of charge, respectively.

B.3. PV Inverters Constraints.

$$-\sqrt{S_j^{\mathrm{PV,cap}} - P_{j,t}^{\mathrm{PV}}} \le Q_{j,t}^{\mathrm{PV}} \le \sqrt{S_j^{\mathrm{PV,cap}} - P_{j,t}^{\mathrm{PV}}}, \quad \forall j \in \mathbf{B}^{a,\mathrm{PV}}, \tag{B.10}$$

where $S_j^{PV,cap}$ is the capacity of PV inverter installed at bus j.

Data Availability

All data used to support the findings of this study are included within the article.

Conflicts of Interest

The authors declare no conflicts of interest.

Acknowledgments

This work was supported by the National Natural Science Foundation of China under Grant 62103254.

References

[1] S. Singh, S. P. Singh, and V. Babu Pamshetti, "Energy efficiency and peak load management via CVR and distributed energy storage in active distribution grid," *International Transactions On Electrical Energy Systems*, vol. 30, no. 3, Article ID e12224, 2020.

[2] V. B. Pamshetti, S. Singh, and S. P. Singh, "Reduction of energy demand via conservation voltage reduction considering network reconfiguration and soft open point," *International Transactions On Electrical Energy Systems*, vol. 30, no. 1, Article ID e12147, 2020.

[3] T. Ding, C. Li, Y. Yang, J. Jiang, Z. Bie, and F. Blaabjerg, "A two-stage robust optimization for centralized-optimal dispatch of photovoltaic inverters in active distribution networks," *IEEE Transactions on Sustainable Energy*, vol. 8, no. 2, pp. 744–754, 2016.

[4] C. Zhang, Z. Dong, and L. Yang, "A feasibility pump based solution algorithm for two-stage robust optimization with integer recourses of energy storage systems," *IEEE Transactions on Sustainable Energy*, vol. 12, no. 3, pp. 1834–1837, 2021.

[5] S. Choi, "Practical coordination between day-ahead and real-time optimization for economic and stable operation of distribution systems," *IEEE Transactions on Power Systems*, vol. 33, no. 4, pp. 4475–4487, 2017.

[6] D. T. Van, S. Chaitusaney, and H. T. Nguyen, "Linear least-squares method for conservation voltage reduction in distribution systems with photovoltaic inverters," *IEEE Transactions on Smart Grid*, vol. 8, no. 3, pp. 1252–1263, 2016.

[7] C. Zhang, Y. Xu, Z. Y. Dong, and J. Ravishankar, "Three-stage robust inverter-based voltage/var control for distribution networks with high-level PV," *IEEE Transactions on Smart Grid*, vol. 10, no. 1, pp. 782–793, 2017.

[8] Y. Xu, Z. Y. Dong, R. Zhang, and D. J. Hill, "Multi-timescale coordinated voltage/var control of high renewable-penetrated distribution systems," *IEEE Transactions on Power Systems*, vol. 32, no. 6, pp. 4398–4408, 2017.

[9] M. J. E. Alam, K. M. Muttaqi, and D. Sutanto, "Mitigation of rooftop solar PV impacts and evening peak support by managing available capacity of distributed energy storage systems," *IEEE Transactions on Power Systems*, vol. 28, no. 4, pp. 3874–3884, 2013.

[10] C. Zhang and Y. Xu, "Hierarchically-coordinated voltage/VAR control of distribution networks using PV inverters," *IEEE Transactions on Smart Grid*, vol. 11, no. 4, pp. 2942–2953, 2020.

[11] Z. Wang, H. Chen, J. Wang, and M. Begovic, "Inverter-less hybrid voltage/var control for distribution circuits with photovoltaic generators," *IEEE Transactions on Smart Grid*, vol. 5, no. 6, pp. 2718–2728, 2014.

[12] P. Rui, C. Zhang, Y. Xu, and Z. Y. Dong, "Rolling horizon based multi-objective robust voltage/VAR regulation with conservation voltage reduction in high PV-penetrated distribution networks," *IET Generation, Transmission & Distribution*, vol. 13, no. 9, pp. 1621–1629, 2019.

[13] E. De Din, F. Bigalke, M. Pau, F. Ponci, and A. Monti, "Analysis of a Multi-timescale framework for the voltage control of active distribution grids," *Energies*, vol. 14, no. 7, p. 1965, 2021.

[14] R. A. Jabr and I. Dzafic, "Sensitivity-based discrete coordinate-descent for volt/var control in distribution networks," *IEEE Transactions on Power Systems*, vol. 31, no. 6, pp. 4670–4678, 2016.

[15] C. Luo, H. Wu, Y. Zhou, Y. Qiao, and M. Cai, "Network partition-based hierarchical decentralised voltage control for distribution networks with distributed PV systems," *International Journal of Electrical Power & Energy Systems*, vol. 130, no. 2021, Article ID 106929, 2021.

[16] M. Bahramipanah, R. Cherkaoui, and M. Paolone, "Decentralized voltage control of clustered active distribution network by means of energy storage systems," *Electric Power Systems Research*, vol. 136, no. 2016, pp. 370–382, 2016.

[17] Y. Chai, L. Guo, C. Wang, Y. Liu, and Z. Zhao, "Hierarchical distributed voltage optimization method for HV and MV distribution networks," *IEEE Transactions on Smart Grid*, vol. 11, no. 2, pp. 968–980, 2019.

[18] R. Majumder, "Aspect of voltage stability and reactive power support in active distribution," *IET Generation, Transmission & Distribution*, vol. 8, no. 3, pp. 442–450, 2014.

[19] Y. Chai, L. Guo, C. Wang, Z. Zhao, X. Du, and J. Pan, "Network partition and voltage coordination control for distribution networks with high penetration of distributed PV units," *IEEE Transactions on Power Systems*, vol. 33, no. 3, pp. 3396–3407, 2018.

[20] P. Li, C. Zhang, Z. Wu, Y. Xu, M. Hu, and Z. Dong, "Distributed adaptive robust voltage/var control with network partition in active distribution networks," *IEEE Transactions on Smart Grid*, vol. 11, no. 3, pp. 2245–2256, 2019.

[21] M. Bazrafshan and N. Gatsis, "Decentralized stochastic optimal power flow in radial networks with distributed generation," *IEEE Transactions on Smart Grid*, vol. 8, no. 2, pp. 787–801, 2017.

[22] Q. Alsafasfeh, O. A. Saraereh, I. Khan, and B. J. Choi, "A robust decentralized power flow optimization for dynamic PV system," *IEEE Access*, vol. 7, pp. 63789–63800, 2019.

[23] P. Li, B. Jin, D. Wang, and B. Zhang, "Distribution system voltage control under uncertainties using tractable chance constraints," *IEEE Transactions on Power Systems*, vol. 34, no. 6, pp. 5208–5216, 2018.

[24] D. Cao, J. Zhao, W. Hu et al., "Data-driven multi-agent deep reinforcement learning for distribution system decentralized voltage control with high penetration of PVs," *IEEE Transactions on Smart Grid*, vol. 12, no. 5, pp. 4137–4150, 2021.

[25] B. Zhang, A. Y. S. Lam, A. D. Domínguez-García, and D. Tse, "An optimal and distributed method for voltage regulation in power distribution systems," *IEEE Transactions on Power Systems*, vol. 30, no. 4, pp. 1714–1726, 2014.

[26] Y. Zhang, T. Yang, and Z. Tang, "Active fault-tolerant control for load frequency control in multi-area power systems with physical faults and cyber attacks," *International Transactions On Electrical Energy Systems*, vol. 31, no. 7, Article ID e12906, 2021.

[27] Y. Fujimoto, M. Fujita, and Y. Hayashi, "Deep reservoir architecture for short-term residential load forecasting: an online learning scheme for edge computing," *Applied Energy*, vol. 298, Article ID 117176, 2021.

[28] T. Pu, X. Wang, Y. Cao et al., "Power flow adjustment for smart microgrid based on edge computing and multi-agent deep reinforcement learning," *Journal of Cloud Computing: Advances, Systems and Applications*, vol. 10, no. 1, pp. 1–13, 2021.

[29] L. Shen, X. Dou, H. Long, C. Li, Ji Zhou, and K. Chen, "Cloud-Edge cooperative dispatching method for distribution networks considering photovoltaic generation uncertainty," *Journal of Modern Power Systems and Clean Energy*, vol. 9, 2020.

[30] Y. Zhang, C. Peng, S. Xie, and X. Du, "Deterministic network calculus-based H∞ load frequency control of multi-Area power systems under malicious DoS attacks," *IEEE Transactions on Smart Grid*, 2021.

[31] C. Lee, S.-H. Kim, and C.-H. Youn, "Cooperating edge cloud-based hybrid online learning for accelerated energy data stream processing in load forecasting," *IEEE Access*, vol. 8, pp. 199120–199132, 2020.

[32] C. Feng, Z. Li, M. Shahidehpour, F. Wen, W. Liu, and X. Wang, "Decentralized short-term voltage control in active power distribution systems," *IEEE Transactions on Smart Grid*, vol. 9, no. 5, pp. 4566–4576, 2017.

[33] M. Zeraati, M. E. H. Golshan, and J. M. Guerrero, "A consensus-based cooperative control of PEV battery and PV active power curtailment for voltage regulation in distribution networks," *IEEE Transactions on Smart Grid*, vol. 10, no. 1, pp. 670–680, 2017.

[34] M. Zeraati, M. E. Hamedani Golshan, and J. M. Guerrero, "Distributed control of battery energy storage systems for voltage regulation in distribution networks with high PV penetration," *IEEE Transactions on Smart Grid*, vol. 9, no. 4, pp. 3582–3593, 2018.

[35] Y. Guo, Q. Wu, H. Gao, and F. Shen, "Distributed voltage regulation of smart distribution networks: consensus-based information synchronization and distributed model predictive control scheme," *International Journal of Electrical Power & Energy Systems*, vol. 111, pp. 58–65, 2019.

[36] F. Li, X. Li, T. Ding, H. Sun, and R. Bo, "Interval radial power flow using extended DistFlow formulation and Krawczyk iteration method with sparse approximate inverse preconditioner," *IET Generation, Transmission & Distribution*, vol. 9, no. 14, pp. 1998–2006, 2015.

[37] W. H. Kersting, "Radial distribution test feeders," *IEEE Transactions on Power Systems*, vol. 6, no. 3, pp. 975–985, 1991.

[38] S. Long, W. Long, Z. Li, K. Li, Y. Xia, and Z. Tang, "A game-based approach for cost-aware task assignment with QoS constraint in collaborative edge and cloud environments," *IEEE Transactions on Parallel and Distributed Systems*, vol. 32, no. 7, pp. 1629–1640, 2021.

[39] C. Fancy and M. Pushpalatha, "Intelligence-enabled approach for load balancing in software-defined data center networks," *International Journal of Communication Systems*, vol. 34, no. 9, Article ID e4818, 2021.